Inorg. Chem. **2009**, *48*, 2078−2093

Structural, Spectroscopic, and Kinetic Investigation of the Molybdenum Dialkylhydrazido Complexes $[MoBr(NNC_5H_{10})(dppe)_2]Br$ and $[Mo(NNC_5H_{10})(dppe)_2]$: Activation Parameters and Revised Mechanism for N−N Cleavage†

Ameli Dreher,‡ Klaus Mersmann,‡ Christian Näther,‡ Ivana Ivanovic-Burmazovic,*,§ Rudi van Eldik,*,§ and Felix Tuczek*,‡

Institut für Anorganische Chemie, Christian-Albrechts-Universität Kiel, Max-Eyth-Strasse 2, 24098 Kiel, Germany, and Anorganische Chemie, Department Chemie and Pharmazie, Friedrich-Alexander Universität Erlangen-Nürnberg, Egerlandstrasse 1, 91058 Erlangen, Germany

Received October 14, 2008

The reaction of $[Mo(NNC_5H_{10})(dppe)_2]$ ($\mathbf{B}^{Mo}$) with an excess of acid, $HNEt_3BPh_4$, is investigated applying temperature-dependent stopped-flow measurements. The kinetic data indicate a biphasic process with rate constants $k_{obs(1)}$ and $k_{obs(2)}$ which are both slower than the single rate constant reported by Henderson et al. (Henderson, R. A.; Leigh, G. J.; Pickett, C. J., *J. Chem. Soc., Dalton Trans.* **1989**, 425−430). Moreover, both rate constants exhibit a linear dependence on the acid concentration with a large intercept which is attributed to acid-dependent and acid-independent components of each reaction phase, respectively. All four reaction channels exhibit temperature-dependent reaction rates. Furthermore, $\mathbf{B}^{Mo}$ and its Mo(IV) analogue $[MoBr(NNC_5H_{10})(dppe)_2]Br$ ($\mathbf{A}^{Mo}$) are characterized structurally and spectroscopically. Density-functional theory calculations are performed to locate possible barriers in the overall reaction scheme and determine their energies, providing additional information for the formulation of a mechanism. The temperature-dependent rate of N−N cleavage is explained by a revised mechanism which involves an α-protonated intermediate that is inert with respect to N−N cleavage and is generated from its β-protonated counterpart by a rapid 1,2-proton shift. The implications of these results with respect to N_2 reduction in the Chatt cycle and the enzyme nitrogenase are discussed.

I. Introduction

The exploration of the different scenarios for synthetic nitrogen fixation—the conversion of N_2 to ammonia under ambient conditions—is a fascinating and actively studied area of modern coordination and organometallic chemistry.[1−6] A central step in all of these reactions is the cleavage of the N−N bond. Besides the direct, transition-metal assisted cleavage of N_2, the N−N bond of coordinated dinitrogen can be split after protonation and/or alkylation.[7−15] This strategy also applies to the reduction and protonation of end-on terminally bound dinitrogen.[16,17] For this chemistry two reactive pathways have been established, the Schrock and the Chatt cycle. Yandulov and Schrock were the first to

† Reduction and Protonation of End-On Coordinated Dinitrogen. VII. Dedicated to Prof. Dr. Gerald Henkel on the occasion of his 60th birthday.

* To whom correspondence should be addressed. E-mail: ivanovic@chemie.uni-erlangen.de (I.I.B), vaneldik@chemie.uni-erlangen.de (R.vE.), ftuczek@ac.uni-kiel.de (F.T.).

‡ Christian Albrechts Universität.

§ Friedrich-Alexander Universität Erlangen-Nürnberg.

(1) MacKay, B. A.; Fryzuk, M. D. *Chem. Rev.* **2004**, *104*, 385–401.
(2) Kozak, C. M.; Mountford, P. *Angew. Chem., Int. Ed.* **2004**, *43*, 1186–1189.
(3) Hidai, M. *Coord. Chem. Rev.* **1999**, *186*, 99–108.
(4) Hidai, M.; Mizobe, Y. *Chem. Rev.* **1995**, *95*, 1115–1133.
(5) Henderson, R. A.; Leigh, G. J.; Pickett, C. J. *Adv. Inorg. Chem.* **1983**, *27*, 197–292.
(6) Chatt, J.; Dilworth, J. R.; Richards, R. L. *Chem. Rev.* **1978**, *78*, 589–625.
(7) Fryzuk, M. D.; Love, J. B.; Rettig, S. J.; Young, V. G. *Science* **1997**, *275*, 1445–1447.
(8) Hussain, W.; Leigh, G. J.; Pickett, C. J. *J. Chem. Soc., Chem. Commun.* **1982**, 747–748.
(9) Ishino, H.; Tokunaga, S.; Seino, H.; Ishii, Y.; Hidai, M. *Inorg. Chem.* **1999**, *38*, 2489–2496.
(10) Le Grand, N.; Muir, K. W.; Petillon, F. Y.; Pickett, C. J.; Schollhammer, P.; Talarmin, J. *Chem. Eur. J.* **2002**, *8*, 3115–3127.
(11) Pickett, C. J.; Leigh, G. J. *J. Chem. Soc., Chem. Commun.* **1981**, 1033–1035.

10.1021/ic801952v CCC: $40.75 © 2009 American Chemical Society
Published on Web 02/03/2009

realize a "truly" catalytic ammonia synthesis, meaning that the amount of converted dinitrogen (in moles) exceeds that of the employed transition-metal complex. Their system is based on the Mo(III) triamidoamine complex [Mo(HIPT)$_3$] which upon reduction with decamethylchromocene and protonation with a lutidinium salt gives ammonia from N_2 in 6 cycles with a yield of 65%.[18,19] The Chatt cycle, on the other hand, involves the conversion of N_2 to NH_3 on the basis of molybdenum and tungsten diphosphine complexes.[20−22] Although no truly catalytic formation of ammonia has been achieved with this system, it provided the first rational and complete scheme for dinitrogen reduction. In particular, dinitrogen, diazenido(-), "hydrazido(2-)", and hydrazidium complexes [M(N$_2$)$_2$(diphos)$_2$], [MX(NNH)(diphos)$_2$], [MX(NNH$_2$)(diphos)$_2$]$^+$, and [MX(NNH$_3$)(diphos)$_2$]$^{2+}$ (M = Mo/W; diphos = 1,2-bis(diethylphosphino)ethane (depe) or 1,2-bis(diphenylphosphino)ethane (dppe); X = Hal, HSO_4, and so forth) have been isolated and characterized.[5,23−25] We have investigated these intermediates with the help of vibrational and optical spectroscopy coupled to density-functional theory (DFT) calculations.[26]

The next step toward the generation of NH_3, the cleavage of the N−N bond, requires the addition of two electrons from an external source.[7−14] The resulting Mo(II) hydrazido(2-) species reacts with acid to give the nitrido complex and ammonia. Mechanistic insight into this process has been obtained using alkylated derivatives.[9,27] In particular, the N−N cleavage reaction of the alkylhydrazido complex [Mo(NNC$_5$H$_{10}$)(dppe)$_2$] (**B**^{Mo}) has been studied by Henderson et al.[27] This complex can be generated by reaction of the analogous Mo(IV) complex [MoBr(NNC$_5$H$_{10}$)(dppe)$_2$]Br (**A**^{Mo}) with *tert*-butyllithium. For the reaction of **B**^{Mo} with $HNEt_3BPh_4$ in nitriles at 25 °C, stopped-flow experiments were performed. The first part of the reaction (initial protonation and solvent coordination) was, however, too fast to be observable with this technique. Nevertheless, the actual N−N cleavage step could be monitored kinetically. The resulting rate constant k_{obs} was found to depend on the acid concentration, exhibiting a saturation behavior with a limiting value of 58.2 s^{-1} for an acid concentration of 20 mmol L^{-1}

Scheme 1

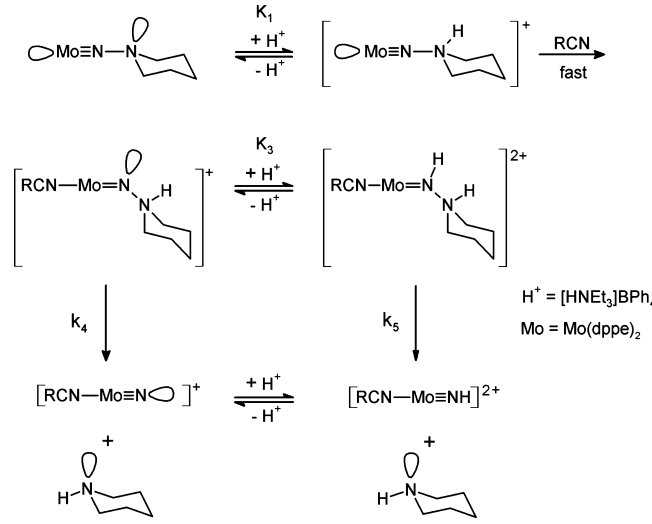

(complex concentration 0.25 mmol L^{-1}). These findings were interpreted in terms of the kinetic scheme shown in Scheme 1 where the acid-independent and acid-dependent N−N cleavage rates are denoted by k_4 and k_5, respectively.

To obtain information with respect to the dependence of the N−N cleavage reaction on the central atom, we recently investigated the protolytic N−N cleavage of the tungsten analogue of **B**^{Mo}, [W(NNC$_5$H$_{10}$)(dppe)$_2$] (**B**^{W}). First, the spectroscopic properties and electronic structures of **B**^{W} and its W(IV) analogue **A**^{W} were evaluated and compared to those of their Mo counterparts **B**^{Mo} and **A**^{Mo}, respectively. A single-crystal X-ray structure determination of the five-coordinate W(II) complex **B**^{W} was reported, and the vibrational properties of compound **A**^{W} and **B**^{W} were evaluated. Infrared and Raman data were analyzed using a Quantum-chemistry assisted normal coordinate analysis (QCA-NCA). Thereby it was found that the N−N force constant decreases from 6.95 to 6.40 mdyn/Å upon going from **A**^{W} to **B**^{W} which corresponds to a change from an N−N double bond to an intermediate between double bond and single bond. Interestingly, also the metal-N force constant decreases (from 5.73 to 4.87 mdyn/Å), which can be understood by the increase in electronic charge on the metal atom upon two-electron reduction. Finally, the molecular orbital (MO) schemes of compounds **A**^{M} and **B**^{M} (M = Mo,W) were determined using DFT, with special emphasis on the nature of the frontier orbitals.[28]

Then, the N−N cleavage reaction of the dialkylhydrazido complex **B**^{W} upon treatment with acid, leading to the nitrido complex and piperidine, was investigated experimentally and theoretically.[29] Most importantly, **B**^{W} was found to react orders of magnitude faster with $HNEt_3BPh_4$ in nitrile solvents at room temperature than its Mo analogue, **B**^{Mo}. Therefore stopped-flow experiments were performed at −70 °C for the reaction of **B**^{W} with $HNEt_3BPh_4$ in propionitrile. Evaluation

(12) Pool, J. A.; Lobkovsky, E.; Chirik, P. J. *Nature* **2004**, *427*, 527–530.
(13) Schrock, R. R.; Glassman, T. E.; Vale, M. G.; Kol, M. *J. Am. Chem. Soc.* **1993**, *115*, 1760–1772.
(14) Smith, J. M.; Lachicotte, R. J.; Holland, P. L. *J. Am. Chem. Soc.* **2003**, *125*, 15752–15753.
(15) Sadique, A. R.; Gregory, E. A.; Brennessel, W. W.; Holland, P. L. *J. Am. Chem. Soc.* **2007**, *129*, 8112–8121.
(16) Lehnert, N.; Tuczek, F. *Inorg. Chem.* **1999**, *38*, 1659–1670.
(17) Lehnert, N.; Tuczek, F. *Inorg. Chem.* **1999**, *38*, 1671–1682.
(18) Yandulov, D. V.; Schrock, R. R. *Science* **2003**, *301*, 76–78.
(19) Yandulov, D. V.; Schrock, R. R. *Inorg. Chem.* **2005**, *44*, 5542–5542.
(20) Chatt, J.; Pearman, A. J.; Richards, R. L. *J. Chem. Soc., Dalton Trans.* **1976**, 1520–1524.
(21) Tuczek, F.; Lehnert, N. *Angew. Chem., Int. Ed.* **1998**, *37*, 2636–2638.
(22) Chatt, J.; Pearman, A. J.; Richards, R. L. *Nature* **1975**, *253*, 39–40.
(23) Tuczek, F.; Horn, K. H.; Lehnert, N. *Coord. Chem. Rev.* **2003**, *245*, 107–120.
(24) Leigh, G. J. *Acc. Chem. Res.* **1992**, *25*, 177–181.
(25) Galindo, A.; Hills, A.; Hughes, D. L.; Richards, R. L.; Hughes, M.; Mason, J. *J. Chem. Soc., Dalton Trans.* **1990**, 283–288.
(26) Horn, K. H.; Lehnert, N.; Tuczek, F. *Inorg. Chem.* **2003**, *42*, 1076–1086.
(27) Henderson, R. A.; Leigh, G. J.; Pickett, C. J. *J. Chem. Soc., Dalton Trans.* **1989**, 425–430.
(28) Horn, K. H.; Böres, N.; Lehnert, N.; Mersmann, K.; Näther, C.; Peters, G.; Tuczek, F. *Inorg. Chem.* **2005**, *44*, 3016–3030.
(29) Mersmann, K.; Horn, K. H.; Böres, N.; Lehnert, N.; Studt, F.; Paulat, F.; Peters, G.; Ivanovic-Burmazovic, I.; van Eldik, R.; Tuczek, F. *Inorg. Chem.* **2005**, *44*, 3031–3045.

of the kinetic data indicated biphasic behavior, which was interpreted in the following way: protonation of $\mathbf{B}^{W}$ is completed within the dead time of the stopped-flow apparatus, leading to the primary protonated intermediate $\mathbf{B}^{W}H^{+}$. Propionitrile coordination to this species proceeds at −70 °C with a rate constant $k_{obs(1)}$ of 1.5 ± 0.4 s^{-1}, generating the intermediate RCN-$\mathbf{B}^{W}H^{+}$ (R = Et) that subsequently mediates N−N bond splitting in a slower reaction ($k_{obs(2)}$ = 0.35 ± 0.08 s^{-1}, 6 equiv of acid). Obviously these findings differ from the results reported for $\mathbf{B}^{Mo}$, where only *one* reaction phase corresponding to the N−N cleavage step had been observed.[27] Moreover, $k_{obs(1)}$ and $k_{obs(2)}$ for $\mathbf{B}^{W}$ were found to be independent of the acid concentration, again in contrast to the Mo system, where an acid-dependent rate constant had been observed. This suggests that in the W system the protonation equilibrium, which corresponds to K_3 shown in Scheme 1 for the Mo system, is already saturated at low acid concentrations, demonstrating a higher activation in $\mathbf{B}^{W}$ than in $\mathbf{B}^{Mo}$ toward N−N cleavage.

DFT calculations were performed on Mo model complexes to understand the experimentally observed reactivities of $\mathbf{B}^{Mo}$ or $\mathbf{B}^{W}$ with acids in nitrile solvents.[29] The quality of these calculations was checked by a comparison between measured and calculated vibrational frequencies. The N−N cleavage of $\mathbf{B}^{Mo}$ and $\mathbf{B}^{W}$ upon reaction with protons was simulated theoretically. It was found that this process is strongly exothermic. Moreover, geometry optimization of a solvent-coordinated, N_β-protonated Mo dialkylhydrazido intermediate was found to spontaneously lead to separation into the nitrido complex and piperidine, corresponding to an activationless, heterolytic N−N bond cleavage process. Finally, DFT also indicated a spontaneous cleavage of solvent-coordinated $\mathbf{B}^{Mo}$ and $\mathbf{B}^{W}$ protonated at N_α *and* N_β. These results were difficult to reconcile with the experimental data obtained for $\mathbf{B}^{W}$ which indicated a strong temperature dependence of the N−N cleavage reaction (vide supra).

To address this point, the N−N cleavage reaction of the Mo and W dialkylhydrazido complexes $\mathbf{B}^{Mo}$ and $\mathbf{B}^{W}$ is reinvestigated in the present study, with emphasis on measuring its temperature dependence and determining the corresponding activation parameters. To this end the reaction of the molybdenum complex $\mathbf{B}^{Mo}$ with acid is studied in a temperature interval ranging from −35 to +15 °C. Note that only for this complex the reaction rates are in a regime where stopped-flow kinetics can be applied; for the W complex the corresponding rates become too fast if the temperature is raised above −70 °C. The obtained data are again interpreted with the help of DFT, complementing the computational results obtained in the previous investigation.[29] In this context also the IR and Raman spectra of $\mathbf{A}^{Mo}$ and $\mathbf{B}^{Mo}$ are presented and interpreted on the basis of the normal coordinate analysis developed previously for $\mathbf{A}^{W}$ and $\mathbf{B}^{W}$. To understand the mechanistic details of the N−N cleavage process, additional DFT calculations on this reaction in the regime of low acid concentration are performed. On the basis of these new theoretical results a revised scheme for the N−N cleavage reaction of $\mathbf{B}^{Mo}$ and $\mathbf{B}^{W}$ is proposed which accounts for all experimental observations and resolves the mechanistic problems which have emerged in the previous study.[29]

Table 1. Crystal and Refinement Data for Compound $\mathbf{B}^{Mo}$

	$\mathbf{B}^{Mo}$
formula	$C_{57}H_{58}MoN_2P_4$
MW/g·mol^{-1}	990.87
crystal color	black
crystal system	monoclinic
space group	*C*2/*c*
a, Å	16.348 (2)
b, Å	19.974 (2)
c, Å	16.673 (2)
β, Å	108.95 (1)
V, Å^3	5149.1 (7)
temperature, K	220
Z	4
$D_{calcd.}$, g·cm^{-3}	1.278
F(000)	12064
2*θ*-range	4−54°
h/*k*/*l* ranges	−20/20, −25/25, −19/21
μ, mm^{-1}	0.417
measured refl.	21991
$R_{int.}$	0.0540
independent refl.	5504
refl. with I > 2*σ*(I)	4792
refined parameters	314
R_1 [$I > 2\sigma(I)$]	0.0327
wR_2 [all data]	0.0863
GoF	1.023
min./max. res., e·Å^{-3}	0.35/−0.67

II. Experimental and Computational Procedures

A. Sample Preparation. The complexes [MoBr(NNC$_5$H$_{10}$)(dppe)$_2$]-Br ($\mathbf{A}^{Mo}$), [Mo(NNC$_5$H$_{10}$)(dppe)$_2$] ($\mathbf{B}^{Mo}$) and [MoBr$_2$(dppe)$_2$] were prepared according to literature procedures.[11,30,31] Samples were handled under nitrogen or argon atmosphere using Schlenk techniques. All solvents were dried under argon. Triethylammoniumtetraphenylborate was synthesized from a metathesis reaction between ammoniumhydrochloride and sodium tetraphenylborate according to a method described in the literature.[32]

B. X-ray Structure Analysis. Intensity data were collected using a STOE imaging plate diffraction system (IPDS-1) with Mo Kα radiation (cf. Table 1). The structure was solved with direct methods using SHELXS-97, and refinement was performed against F^2 using SHELXL-97.[33] All non-H atoms were refined anisotropically. The hydrogen atoms were positioned with idealized geometry and refined with fixed isotropic displacement parameters using a riding model. The carbon atoms of the dialkylhydrazido ligand are disordered around a 2-fold axis. The structure was also refined in space group *Cc*, where the 2-fold axis is not present. However, the dialkylhydrazido ligand was still disordered and the Flack-X-parameter refined to 0.50 (5). The structure contains solvent accessible voids of about 110 Å^3, which are definitely not filled with solvent. CCDC 696222 contains the supplementary crystallographic data for this paper. These data can be obtained free of charge from the Cambridge Crystallographic Data Center via www.ccdc.cam.uk/data_request.cif.

(30) Chatt, J.; Hussain, W.; Leigh, G. J.; Terreros, F. P. *J. Chem. Soc., Dalton Trans.* **1980**, 1408–1415.
(31) Al-Salih, T. I.; Pickett, C. J. *J. Chem. Soc., Dalton Trans.* **1985**, 1255–1264.
(32) Rodima, T.; Kaljurand, I.; Pihl, A.; Maemets, V.; Leito, I.; Koppel, I. A. *J. Org. Chem.* **2002**, *67*, 1873–1881.
(33) Sheldrick, G. M. *SHELXS-97 and SHELXL-97: Program for the Solution and Refinement of Crystal Structures*; University of Göttingen: Göttingen, Germany, 1997.

C. NMR Spectroscopy. NMR spectra were recorded on a Bruker Avance 400 Pulse Fourier transform spectrometer operating at a ^{1}H frequency of 400.13 MHz using a 5 mm inverse triple-resonance probe head. Referencing was done with TMS $\delta_{1H} = 0$ ppm as substitutive standard. The sample was measured in CD_2Cl_2 at 300 K.

D. IR Spectroscopy. Middle-infrared spectra (MIR) were obtained from KBr pellets using a Mattson Genesis type I spectrometer at 10 K. The spectra were recorded from 4000−40 cm^{-1} with a resolution of 2 cm^{-1}.

E. Raman Spectroscopy. For the Raman spectra of $\mathbf{A}^{Mo}$ and $[MoBr_{2(}dppe)_2]$ a NIR-FT-Raman spectrometer IFS 66/CS with a Bruker FRA 106 module was used. The radiation source was a 350 mW-NdYAG-Laser with a wavelength of 1064 nm. Resonance Raman spectra of $\mathbf{B}^{Mo}$ were recorded with a DILOR XY-multichannel Raman spectrometer with a triple monochromator and a CCD detector. Excitation wavelengths between 454.5 and 647.1 nm were generated by an Ar^+/Kr^+ laser. The resolution was between 2.5 and 0.8 cm^{-1} depending on the wavelength.

F. Stopped-Flow Measurements. Concentration- and temperature-dependent kinetic data were obtained by recording time-resolved UV/vis spectra using a modified Bio-Logic stopped-flow module μSFM-20 instrument combined with a cryo-stopped-flow accessory (Huber CC90 cryostat) and equipped with a J & M TIDAS high-speed diode array spectrometer with a combined deuterium and tungsten lamp (200−1015 nm bandwidth). Isolast O-rings were used for all sealing purposes. The Bio-Logic stopped-flow system is especially designed for oxygen sensitive experiments, having an excellent sealing system and enabling N_2 or Ar to be purged through the system, that is, through the syringe- and mixing-blocks, and through the tubing system. To further exclude the possibility of any O_2 leakage, we performed measurements in the apparatus without injecting acid and observed no spectral change with respect to the spectrum of original compound $\mathbf{B}^{Mo}$. Concentration-dependent measurements were performed in acetonitrile by mixing a solution of $\mathbf{B}^{Mo}$ (the complex concentration was kept constant, [complex] = 0.25 mM) with an excess of $[HNEt_3]BPh_4$ in a 1:1 volume ratio. Data were analyzed using the integrated Bio-Kine software version 4.23 and the Specfit/32 program.

Complete time-dependent spectra were taken for every temperature and acid concentration. The time evolution was fitted to a sequential reaction pathway B → C → D; that is, every time-dependent spectrum is considered as composed of the initial spectrum (B), the final spectrum (D) and the spectrum of the intermediate (C). Each "run" (i.e., stopped-flow experiment for one concentration and one temperature) was analyzed like this (with no restrictions applied), giving two kinetic constants ($k_{obs(1)}$ and $k_{obs(2)}$) and a spectrum of the intermediate (C); cf. Supporting Information. Typically rate constants obtained from four runs under identical conditions were averaged. The fact that almost identical spectra of the intermediate (C) were obtained under different conditions supports the applied model of two consecutive reaction steps.

G. DFT Calculations. DFT calculations have been made for the completion of the calculation in the earlier article, employing the same methodology (functional and basis set) as described in this article.[29] To avoid abstracting a phosphor-bonded proton DFT calculations were performed for the solvent-coordinated and protonated derivatives of $[Mo(NNC_5H_{10})((CH_3)_2PC_2H_4P(CH_3)_2)]$ ($\mathbf{B}_{dmpe}$) instead of the model complex $[Mo(NNC_5H_{10})(PH_2C_2H_4PH_2)_2]$ ($\tilde{\mathbf{B}}$) using B3LYP with the LANL2DZ basis set.[34−38] All computational procedures were used as implemented in the Gaussian 03 package.[39]

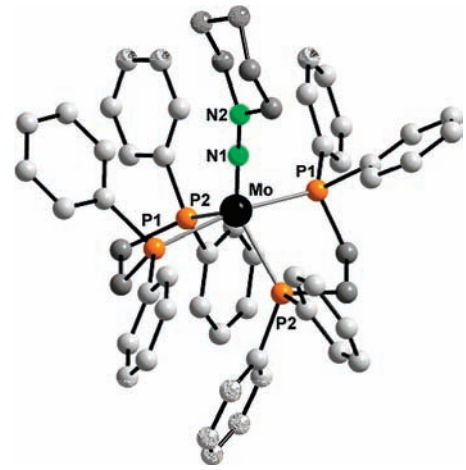

Figure 1. Crystal Structure of B^{Mo}.

III. Structural and Spectroscopic Investigation of A^{Mo} and B^{Mo}

A. X-ray Structure Analysis of B^{Mo}. The structure of the molybdenum dialkylhydrazido complex $\mathbf{B}^{Mo}$ is shown in Figure 1; the most important bond lengths and angles are collected in Table 2, center column. As expected, the structure is very similar to that of the W analogue $\mathbf{B}^{W}$ whose structure has been presented before.[28] In the W complex the metal atom is coordinated by four P atoms of two dppe ligands and N_α (N(1)) of the hydrazido ligand in a distorted trigonal-bipyramidal geometry with P(1) and P(4) in axial and P(2), P(3), and N(1) in equatorial positions (cf. Table 2). The Mo analogue $\mathbf{B}^{Mo}$ exhibits the same coordination geometry with P(1) and P(1A) in axial and P(2), P(2A) and N(1) in equatorial positions (cf. Figure 1). The axial P(1A)−Mo−P(1) angle is 167° and larger than the corresponding P(1)−W−P(4) angle in the tungsten complex (157°) whereas the equatorial P(2A)−Mo−P(2) angle in $\mathbf{B}^{Mo}$ is 105° and thus smaller than in $\mathbf{B}^{W}$ (108°). The metal−N−N bond in $\mathbf{B}^{W}$ is slightly bent (178°), in agreement with the calculation (left column of Table 2). The metal−N−N moiety of $\mathbf{B}^{Mo}$, in contrast, is located on a 2-fold axis and disordered

(34) Becke, A. D. *J. Chem. Phys.* **1993**, *98*, 5648–5652.
(35) Dunning, T. H., Jr.; Hay, P. J. In *Modern Theoretical Chemistry*, 3rd ed.; Schaefer, H. F., Ed.; Plenum: New York, 1976.
(36) Hay, P. J.; Wadt, W. R. *J. Chem. Phys.* **1985**, *82*, 270–283.
(37) Hay, P. J.; Wadt, W. R. *J. Chem. Phys.* **1985**, *82*, 299–310.
(38) Wadt, W. R.; Hay, P. J. *J. Chem. Phys.* **1985**, *82*, 284–298.
(39) Frisch, M. J.; Trucks, G. W.; Schlegel, H. B.; Scuseria, G. E.; Robb, M. A.; Cheeseman, J. R.; Montgomery, J. J. A.; Vreven, T.; Kudin, K. N.; Burant, J. C.; Millam, J. M.; Iyengar, S. S.; Tomasi, J.; Barone, V.; Mennucci, B.; Cossi, M.; Scalmani, G.; Rega, N.; Petersson, G. A.; Nakatsuji, H.; Hada, M.; Ehara, M.; Toyota, K.; Fukuda, R.; Hasegawa, J.; Ishida, M.; Nakajima, T.; Honda, Y.; Kitao, O.; Nakai, H.; Klene, M.; Li, X.; Knox, J. E.; Hratchian, H. P.; Cross, J. B.; Bakken, V.; Adamo, C.; Jaramillo, J.; Gomperts, R.; Stratmann, R. E.; Yazyev, O.; Austin, A. J.; Cammi, R.; Pomelli, C.; Ochterski, J. W.; Ayala, P. Y.; Morokuma, K.; Voth, G. A.; Salvador, P.; Dannenberg, J. J.; Zakrzewski, V. G.; Dapprich, S.; Daniels, A. D.; Strain, M. C.; Farkas, O.; Malick, D. K.; Rabuck, A. D.; Raghavachari, K.; Foresman, J. B.; Ortiz, J. V.; Cui, Q.; Baboul, A. G.; Clifford, S.; Cioslowski, J.; Stefanov, B. B.; Liu, G.; Liashenko, A.; Piskorz, P.; Komaromi, I.; Martin, R. L.; Fox, D. J.; Keith, T.; Al-Laham, M. A.; Peng, C. Y.; Nanayakkara, A.; Challacombe, M.; Gill, P. M. W.; Johnson, B.; Chen, W.; Wong, M. W.; Gonzalez, C.; Pople, J. A. *Gaussian 03*, Revision C.02; Gaussian,Inc.: Wallingford, CT, 2003.

Table 2. Important Bond Distances [Å] and Angles [deg] of $\tilde{\mathbf{B}}^{Mo}$, $\mathbf{B}^{Mo}$, and $\mathbf{B}^{W}$

bond lengths [Å] and angles [deg]	$\tilde{\mathbf{B}}^{Mo}$ geometry optimization[28]	$\mathbf{B}^{Mo}$ X-ray structure	$\mathbf{B}^{W}$ X-ray structure[28]	bond lengths [Å] and angles [deg]
Δ(NN)	1.34	1.324(3)	1.388(7)	Δ(NN)
Δ(MoN)	1.82	1.806(2)	1.781(5)	Δ(WN)
Δ(MoP(1))	2.51	2.446(5)	2.4682(2)	Δ(WP(4))
Δ(MoP(1A))	2.51	2.446(5)	2.4346(2)	Δ(WP(1))
Δ(MoP(2))	2.50	2.406(5)	2.4195(2)	Δ(WP(3))
Δ(MoP(2A))	2.49	2.406(5)	2.3961(2)	Δ(WP(2))
α(N(1)N(2)Mo)	178.7	180.0(Å)	177.9(5)	α(N(2)N(1)W)
α(P(2A)MoP(1))	91.24	92.67(2)	89.7(1)	α(P(2)WP(4))
α(P(2)MoP(1A))	89.29	92.67(2)	87.9(1)	α(P(3)WP(1))
α(P(2A)MoP(1A))	79.8	79.43(2)	77.8(1)	α(P(2)WP(1))
α(P(2)MoP(1))	79.8	79.43(2)	77.6(1)	α(P(3)WP(4))
α(P(1A)MoP(1))	163.5	167.1(1)	157.1(1)	α(P(1)WP(4))
α(P(2A)MoP(2))	105.4	105.2(1)	107.7(1)	α(P(2)WP(3))
α(N(1)MoP(1A))	99.54	96.47(1)	99.3(2)	α(N(2)WP(1))
α(N(1)MoP(1))	96.89	96.47(1)	103.6(2)	α(N(2)WP(4))
α(N(1)MoP(2A))	127.0	127.38(1)	126.3(2)	α(N(2)WP(2))
α(N(1)MoP(2))	127.6	127.38(1)	125.9(2)	α(N(2)WP(3))
α(N(1)N(2)C(1)C(5)) pyramidal angle averaged over all angles of all comformers	118.1	118.0(Å)	112.2(Å)	α(N(2)N(1)C(91)C(95)) pyramidal angle averaged over all angles of all comformers

in two orientations; the Mo−N−N angle thus is determined to 180°.

The structure of $\mathbf{B}^{Mo}$ is well reproduced by the DFT calculations performed on model $\tilde{\mathbf{B}}$;[28] as a matter of fact almost all bond angles of $\tilde{\mathbf{B}}$ listed in Table 2 show a better agreement with those of $\mathbf{B}^{Mo}$ than $\mathbf{B}^{W}$. Whereas the metal−P distances are about equal in both complexes, the tungsten complex exhibits a longer N−N bond (1.39 Å) than its molybdenum counterpart (1.32 Å). The metal-N bond length, in turn, is shorter in the W (1.78 Å) than in the Mo complex (1.81 Å), reflecting a stronger metal−ligand interaction in the W as compared to the Mo complex. The more pronounced single-bond character of the N−N bond in $\mathbf{B}^{W}$ is also borne out by the larger pyramidalization of N_β (sp^3 character) as compared to $\mathbf{B}^{Mo}$. The N−N interaction in $\mathbf{B}^{Mo}$, in contrast, is closer to a double bond, as evident from the larger sp^2-character of N_β. The higher propensity of $\mathbf{B}^{W}$ toward N−N cleavage in comparison to $\mathbf{B}^{Mo}$ thus is clearly explained by characteristic structural differences between these two five-coordinate, divalent dialkylhydrazido complexes, leading to a higher activated N−N unit in $\mathbf{B}^{W}$ as compared to $\mathbf{B}^{Mo}$.

B. NMR-Spectroscopic Analysis of $\mathbf{A}^{Mo}$. The Mo(II) dialkylhydrazido complex $\mathbf{B}^{Mo}$ has been characterized by NMR spectroscopy earlier, demonstrating that it retains its trigonal-bipyramidal in solution. ^{1}H NMR data of $\mathbf{A}^{Mo}$ have been presented by Chatt et al. with the assignment of some broad signals to the alkyl protons of the piperidine ring.[30] We found signals for the aliphatic protons at $\delta = 1.62$ ppm (m, 4H, NCH_2-) and 0.81−0.73 (m, 6H, NCH_2CH_2-, $N(CH_2)_2CH_2$-) (cf. Supporting Information, Figure S1); the aromatic protons cause a signal in the region of 7.54 to 7.06 ppm (40 H). The ^{1}H-^{1}H-COSY45 spectrum (Supporting Information, Figure S2) confirms these assignments, showing the coupling of the four α-C protons (NCH_2-) of the piperidine ring with the four β-C protons (NCH_2CH_2) and the two γ-C protons ($N(CH_2)_2CH_2$-). Furthermore a ^5J-coupling of the two *ortho*-phenyl- proton signals (7.53 ppm and 7.24 ppm) with the -PCH_2-protons can be recognized.

C. Vibrational Spectroscopic Analysis of $\mathbf{A}^{Mo}$. The infrared spectrum of $[MoBr(NNC_5H_{10})(dppe)_2]Br$ ($\mathbf{A}^{Mo}$) is very similar to that of $[WBr(NNC_5H_{10})(dppe)_2]Br$ ($\mathbf{A}^{W}$) which has been determined and interpreted in detail previously (Figure 2a).[28] A comparison of the MIR spectrum of $\mathbf{A}^{Mo}$ with that of the Mo(II) complex $[MoBr_2(dppe)_2]$ is shown in Figure 2b. It is clearly seen that the characteristic vibrations of the dialkylhydrazido(2-) moiety are absent in the spectrum of $[MoBr_2(dppe)_2]$, supporting our earlier assignments. The frequencies of these modes are collected in Table 3. The composition of the modes listed in Table 4 is taken from the vibrational study of $\mathbf{A}^{W}$ for which a normal coordinate analysis (NCA) has been performed (vide supra).[28] To this end the ^{15}N isotopomer of $\mathbf{A}^{W}$ had been investigated as well.

The similarity of the vibrational frequencies indicates that the force field derived for $\mathbf{A}^{W}$ can be applied to $\mathbf{A}^{Mo}$ as well. Because of strong coupling of the N−N stretch with H−C−H bending motions of the piperidine ring ν(NN) is split into three modes, corresponding to bands I, IV, and V (Figure 2). For $\mathbf{A}^{W}$ the main component I has been found to be a combination of ν(NN) (46%) with ν_{12} of the piperidine ring ($\nu(NN)^1$). NCA did not reproduce the splitting of this mode into band Ia and band Ib but led to a value of 1416 cm^{-1} for ^{14}N-$\mathbf{A}^{W}$ with an isotopic shift of −27 cm^{-1}, in good agreement with the combined shifts observed for band Ia and band Ib. The spectrum of $\mathbf{A}^{Mo}$ neither shows any splitting but only exhibits a shoulder at 1412 cm^{-1}. The second component of the N−N stretch is a combination of the HCH twisting mode ν_{25} with $\nu(NN)^2$ (band IV) which was observed at 1236 cm^{-1} for ^{14}N-$\mathbf{A}^{W}$; this band can be found at 1234 cm^{-1} in the spectrum of $\mathbf{A}^{Mo}$. Band V ($\nu(NN)^3$) has been observed at 1125 cm^{-1} with an isotope shift of about −5 cm^{-1} for $\mathbf{A}^{W}$ and has been attributed to ν_{28} admixed with 6% ν(NN) and 4% ν(WN); it is at about the same position in $\mathbf{A}^{Mo}$. The H−C−H-bending vibration ν_{21} was found to be comparable to its position in free piperidine (1351 cm^{-1}) and observed at 1353 cm^{-1} in $\mathbf{A}^{W}$ (band II), where it is also

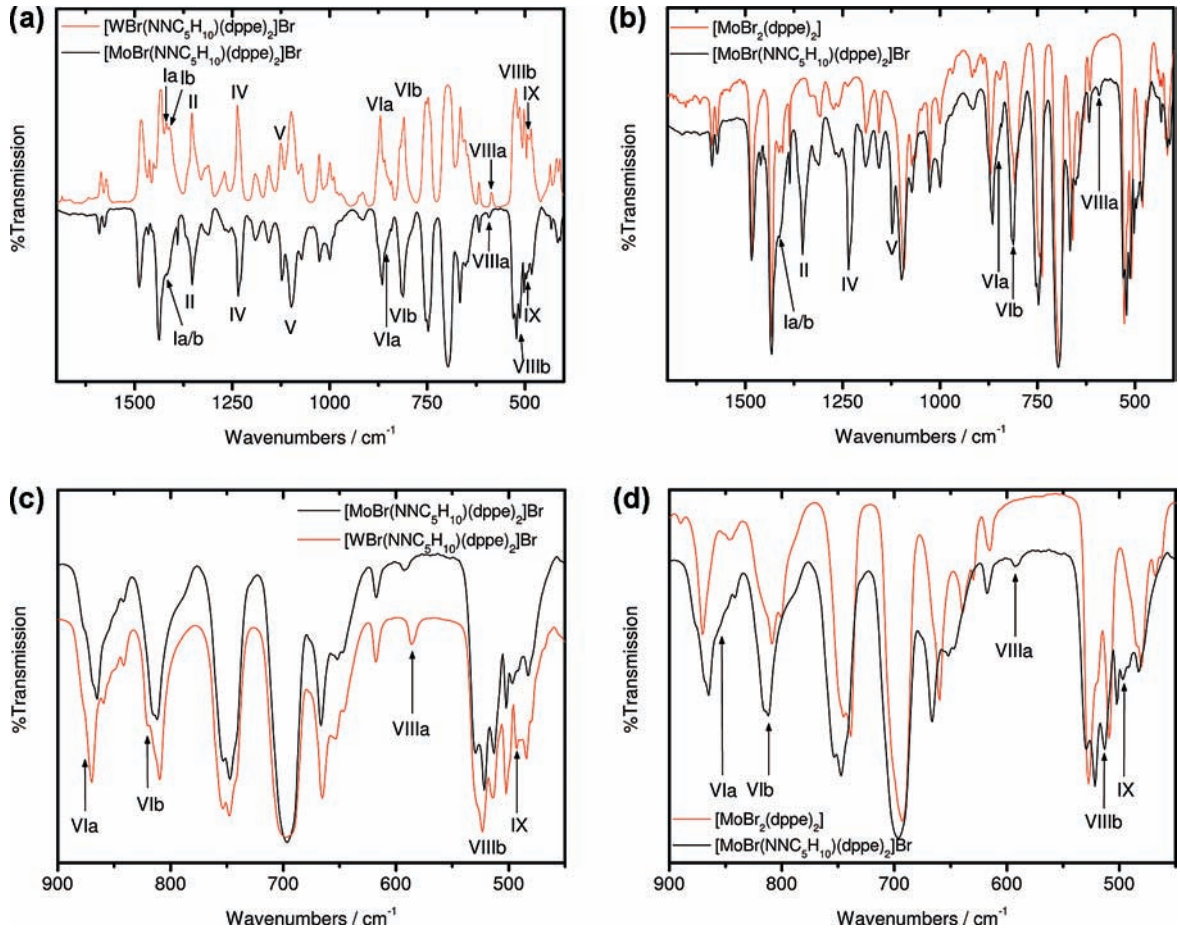

Figure 2. (a) Comparison of the Infrared spectra of $\mathbf{A}^{Mo}$ (transmission, black line) and $\mathbf{A}^{W}$ (absorption, red line).[28] (b) Comparison of the IR spectra of $[MoBr_2(dppe)_2]$ (red line) and $\mathbf{A}^{Mo}$ (black line). (c) Detail of the IR spectra of $\mathbf{A}^{W}$ (red line) and $\mathbf{A}^{Mo}$ (black line).[28] (d) Detail of the IR spectra of $[MoBr_2(dppe)_2]$ (red line) and $\mathbf{A}^{Mo}$ (black line). All spectra were recorded at a temperature of 10 K.

Table 3. Vibrational Frequencies of the Dialkylhydrazido Ligand-Metal Unit Observed in the IR and Raman Spectra of $[MoBr(NNC_5H_{10})(dppe)_2]Br$ ($\mathbf{A}^{Mo}$) and $[WBr(NNC_5H_{10})(dppe)_2]Br$ ($\mathbf{A}^{W}$)($T = 10$ K) in Comparison with the Frequencies Calculated by DFT and Normal Coordinate Analysis[28]

	observed frequences in cm^{-1}					
	$[MoBr(NNC_5H_{10})(dppe)_2]Br$		$[WBr(NNC_5H_{10})(dppe)_2]Br$[28]			
assigment	IR	Raman	IR	Raman	DFT[28]	QCB-NCA[28]
Ia/b	1412	1421	1420/1411	1418/1408	1481/1388	1389
II	1353	1352	1353		1377	1356
III					1271	1276
IV	1234	1237	1236	1237	1260	1228
V	1123	1122	1125	1126	1163	1132
VIa	855	862	874	870	879	860
VIb	812	815	820	821	817	799
VIIIa	592		585		594	573
VIIIb	513		525		506	506
IX	497	499	494		492	481

found in $\mathbf{A}^{Mo}$.[28] The N−C stretching mode (band III), finally, is not visible for $\mathbf{A}^{Mo}$, as in the spectrum of ^{14}N-$\mathbf{A}^{W}$.

In the region from 800−900 cm^{-1} the piperidine ring vibrations ν_{35} and ν_{38} are located which mix with the metal-N stretching vibration. For $\mathbf{A}^{W}$, bands VIa and VIb were observed at 874 and 820 cm^{-1} and assigned to ν_{35} and ν_{38}, admixed with 55% and 15% ν(WN), respectively. The bending vibrations of the linear M−N−N unit split into two orthogonal components, δ^{ip} and δ^{oop} (bands VIIIa and VIIIb). The feature in the spectrum of ^{14}N-$\mathbf{A}^{W}$ at 585 cm^{-1} that shifts to 572 cm^{-1} in the spectrum of ^{15}N-$\mathbf{A}^{W}$ has been assigned to δ^{ip}(WNN); the corresponding out-of-plane component was

Table 4. Assigned Vibrations of the Dialkylhydrazido Ligand-Metal Unit of $\mathbf{A}^{Mo}$

band no.	main character
Ia	ν(NN) + ν_{12}: $\boldsymbol{\nu}$**(NN)**^{1}
II	ν_{21} + ν(NN) + ν(CN)
III	ν_{24} + ν(NN) + $\nu(CN)_{as}$
IV	ν_{25} + ν(NN): $\boldsymbol{\nu}$**(NN)**^{2}
V	ν_{28} + ν(NN): $\boldsymbol{\nu}$**(NN)**^{3}
VIa	ν_{35} + ν(MoN)
VIb	ν_{38} + ν(MoN)
VIIIa	δ^{ip}(MoNN)
VIIIb	δ^{oop}(MNN)
IX	ν_{40} + ν(MoN)

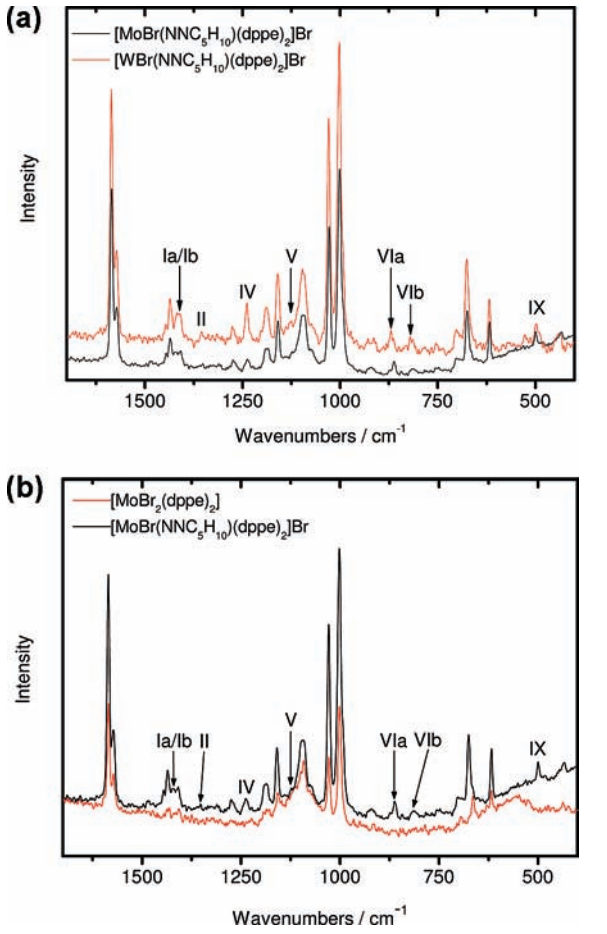

Figure 3. (a) Comparison of the Raman spectra of $\mathbf{A}^{Mo}$ (black line) and $\mathbf{A}^{W}$ (red line).[28] (b) Comparison of the Raman spectra of $MoBr_2(dppe)_2$ (red line) and $\mathbf{A}^{Mo}$ (black line).

determined by NCA to be 521 cm^{-1}. A combination of ν_{40} with ν(WN) (2%) (band IX), finally, was observed at 492 cm^{-1}, exhibiting an isotope shift of -2 cm^{-1}.

For $\mathbf{A}^{Mo}$ the piperidine and metal−nitrogen-vibrations VIa, VIb, VIIIa, VIIIb, and IX can be identified from a comparison between the IR spectra of $\mathbf{A}^{Mo}$ with those of $\mathbf{A}^{W}$ (Figure 2c) and $[MoBr_2(dppe)_2]$ (Figure 2d), respectively (cf. Table 3). Importantly, the metal-N stretching and metal−N−N bending vibrations are slightly shifted to lower frequencies as compared to $\mathbf{A}^{W}$. A comparison of the Raman spectra of $\mathbf{A}^{Mo}$ and $\mathbf{A}^{W}$ is given in Figure 3a, and Figure 3b shows the Raman spectra of $[MoBr_2dppe_2]$ and $\mathbf{A}^{Mo}$. From these Figures the vibrations involving N−N and metal-N motion can clearly be identified; that is, Ia, Ib, II, IV, V, VIa, VIb, IX. The deformation vibration II has so little intensity in $\mathbf{A}^{Mo}$ that it is hardly seen. More intense are the MoN-bands VIa, VIb, and IX, as well as band IV which has NN stretching character (vide supra). Band III that appeared in the IR spectrum of ^{15}N-labeled $\mathbf{A}^{W}$ can neither be found in the IR nor in the Raman spectrum of $\mathbf{A}^{Mo}$, in analogy to the tungsten system.

D. Vibrational Spectroscopic Analysis of $\mathbf{B}^{Mo}$. A comparison of the MIR spectrum of $[Mo(NNC_5H_{10})(dppe)_2]$ ($\mathbf{B}^{Mo}$) with that of $[W(NNC_5H_{10})(dppe)_2]$ ($\mathbf{B}^{W}$) is presented in Figure 4. Again the spectra are found to be very similar.

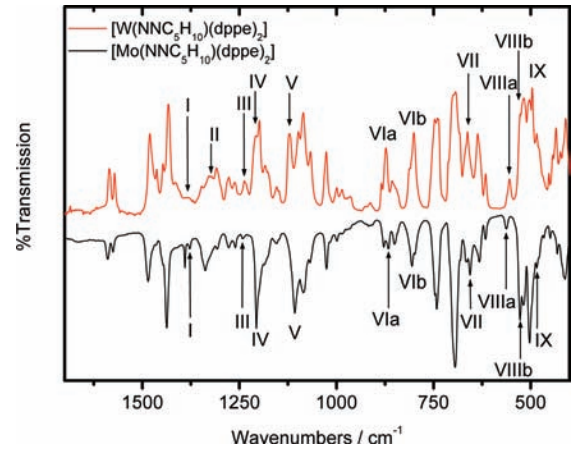

Figure 4. Comparison of the Infrared spectra of $\mathbf{B}^{Mo}$ (transmission, black line) and $\mathbf{B}^{W}$ (absorption, red line). The spectra were recorded at a temperature of 10 K.[28]

Table 5. Comparison of the Observed and Calculated Vibrations in the IR and Raman Spectra of $[Mo(NNC_5H_{10})(dppe)_2]$ ($\mathbf{B}^{Mo}$) and $[W(NNC_5H_{10})(dppe)_2]$ ($\mathbf{B}^{W}$)[a]

	observed frequences in cm^{-1}					
	$[Mo(NNC_5H_{10})(dppe)_2]$		$[W(NNC_5H_{10})(dppe)_2]$[28]			
assignment	IR	Raman	IR	Raman	DFT[28]	QCB-NCA[28]
I	1378		1382		1391	1379
II			1329		1372	1329
III	1242	1269	1237	1236	1270	1242
IV	1206	1204	1208	1203	1243	1214
V	1107	1107	1121	1123	1153	1125
VIa	866	873	873	878	876	865
VIb	805	805	813	813	812	804
VII	657		663		644	635
VIIIa	563	560	554	554	576	557
VIIIb	527		526		500	527
IX	484	491	496		495	483

[a] For the Raman of $\mathbf{B}^{Mo}$ an excitation wavelength of 488 nm was used, for the Raman spectrum of $\mathbf{B}^{W}$ radiation with a wavelength of 1064 nm.[28]

Table 6. Assigned Vibrations of the Dialkylhydrazido Ligand-Metal Unit of $\mathbf{B}^{Mo}$

band no.	main character
I	ν(NN) + ν_{12}: $\boldsymbol{\nu}$**(NN)**^{1}
II	ν_{21}
III	ν_{24} + ν(NN) + $\nu(CN)_{as}$
IV	ν(NN) + ν_{25}: $\boldsymbol{\nu}$**(NN)**^{2}
V	ν(NN) + ν_{28}: $\boldsymbol{\nu}$**(NN)**^{3}
VIa	ν_{35} + ν(MoN)
VIb	ν_{38} + ν(MoN)
VII	ν_{39} + ν(MoN)
VIIIa	δ^{ip}(MoNN)
VIIIb	δ^{oop}(MoNN)
IX	ν_{40} + ν(MoN)

The observed vibrational frequencies of $\mathbf{B}^{Mo}$ and $\mathbf{B}^{W}$, as well as the calculated frequencies, are collected in Table 5; the composition and designation of the vibrational modes according to the normal coordinate analysis of $\mathbf{B}^{W}$ are listed in Table 6. Importantly, band II is not visible in the spectrum of $\mathbf{B}^{Mo}$; only a little shoulder can be observed at 1325 cm^{-1}. All other bands of the dialkylhydrazido ligand of $\mathbf{B}^{Mo}$ can be identified, albeit with different intensities as compared to $\mathbf{B}^{W}$. The NN vibrations of $\mathbf{B}^{Mo}$ (bands I, IV, V) seem to be more intense than in $\mathbf{B}^{W}$, whereas the bands of the metal−nitrogen stretch (VI, VII, IX) show lower intensities. As for $\mathbf{A}^{Mo}$ and $\mathbf{A}^{W}$, spectral comparison of $\mathbf{B}^{Mo}$ and $\mathbf{B}^{W}$ reveals a minimal shift of most metal−nitrogen bands to

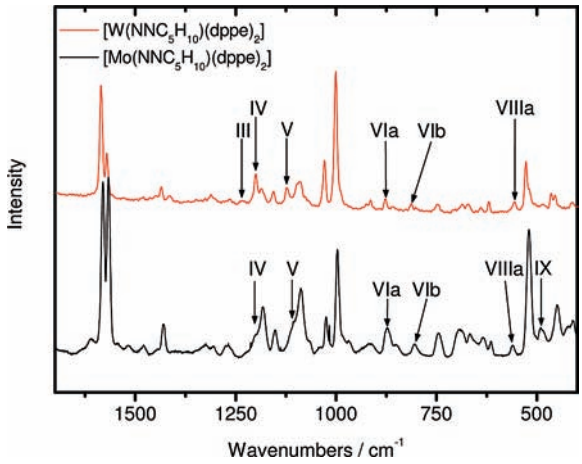

Figure 5. Comparison of the Raman spectra of $\mathbf{B}^{Mo}$ (black line, excitation wavelength of 488 nm) and $\mathbf{B}^{W}$ (red line, excitation wavelength of 1064 nm).[28]

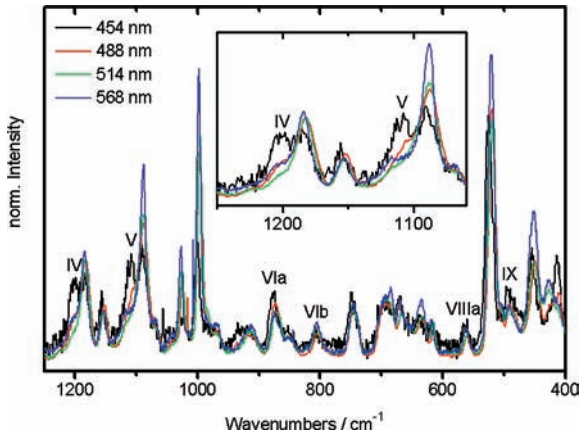

Figure 6. Normalized Raman spectra of $\mathbf{B}^{Mo}$ with different excitation wavelength. Normalization was made to vibrational bands of the dppe ligand. Those relative intensity is unchanged by variation of the excitation wavelength.

lower wavelengths (cf. Table 5). The only bands exhibiting a shift to *higher* frequencies are band III, which in $\mathbf{B}^{Mo}$ is at 5 cm^{-1} higher frequency than in the $\mathbf{B}^{W}$, and band VIIIa (δ^{ip}(MNN)), which is at 7 cm^{-1} higher frequency. The same shift (+6 cm^{-1}) with respect to the tungsten counterpart has also been observed in $\mathbf{A}^{Mo}$ for this vibration.

We also recorded resonance Raman spectra of $\mathbf{B}^{Mo}$. One of these spectra obtained with an excitation wavelength 488 nm is compared with the FT-Raman spectrum of $\mathbf{B}^{W}$ in Figure 5 (for $\mathbf{B}^{Mo}$ an FT-Raman spectrum could not be recorded due to the decomposition of the sample). In Figure 6 the resonance Raman spectra recorded with excitation wavelengths of 454, 488, 514, and 568 nm are collected with normalized intensities. Again the characteristic vibrations of the metal-dialkylhydrazido moiety are visible. Bands IV and V have quite strong intensities in the IR spectrum, but the corresponding peaks are only visible as shoulders in the Raman spectrum in Figure 5. However, they become much more intense at an excitation wavelength of 454 nm. Figure 6 shows that these peaks in fact exhibit the strongest intensity increase of all peaks below 1220 cm^{-1} upon lowering the excitation wavelength from 568 to 454 nm. This suggests

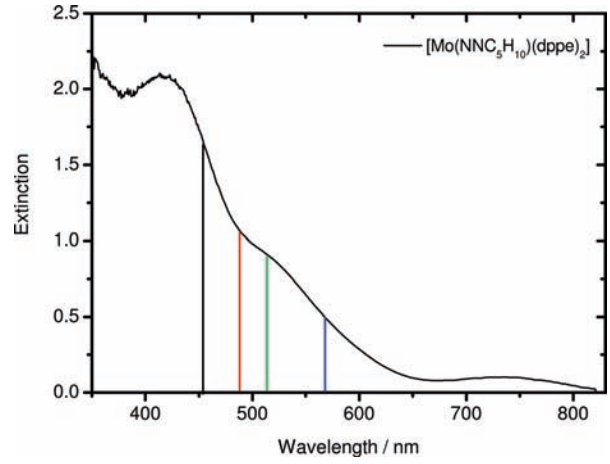

Figure 7. UV/vis spectrum of $\mathbf{B}^{Mo}$ and excitation wavelength of the Resonance Raman spectra. Black line, 454 nm; red line, 488 nm; green line, 514 nm; blue line, 568 nm.

that they are resonance enhanced with respect to an optical absorption band in the UV or near-UV.

Figure 7 shows the UV/vis spectrum of $\mathbf{B}^{Mo}$ along with the different excitation wavelengths of the resonance Raman measurements. The spectrum exhibits an absorption band at 418 nm and a shoulder at ~ 520 nm. Because of the presence of dppe ligands which cause absorption bands in this region of the UV/vis spectrum, these absorption features are difficult to assign. However, the sharp intensity increase of the NN-vibrational bands IV and V if an excitation wavelength is used in the region of the 418 nm band suggests that this optical absorption feature is related to the dialkylhydrazido ligand. On the basis of the MO scheme developed in the previous publication,[28] a probable assignment for this absorption band is a transition from a metal−ligand π bonding combination to the corresponding antibonding combination.

IV. N−N Cleavage of $\mathbf{B}^{Mo}$: Determination of Activation Parameters

A. DFT Calculations on the N−N Cleavage Process: Theoretical Results. Before presenting the experimental data and their interpretation it is useful to explore the energetics of several possible N−N cleavage pathways of compound **B** using DFT. From the calculations and geometry optimizations presented in the earlier study the following results were obtained:[29]

(1) The N_β-protonated, solvent-free intermediate $\mathbf{BH}^+$ spontaneously cleaves the N−N bond. A relaxed potential energy scan (rPES) was performed for this reaction, showing a barrierless profile along the N−N coordinate between the dialkylhydrazidium complex and the separated products (nitrido complex and piperidine).

(2) The N_α-protonated, solvent-free intermediate ($\mathbf{BH}^+_\alpha$), in contrast, is inert toward N−N cleavage. For this reason N_α protonation was discounted as an unproductive side path in the overall reaction scheme (the same holds for the metal-protonated species).

(3) Solvent coordination to the N_β-protonated intermediate $\mathbf{BH}^+$ is quite exergonic (−17 kcal/mol), but requires an activation energy of 16 kcal/mol.

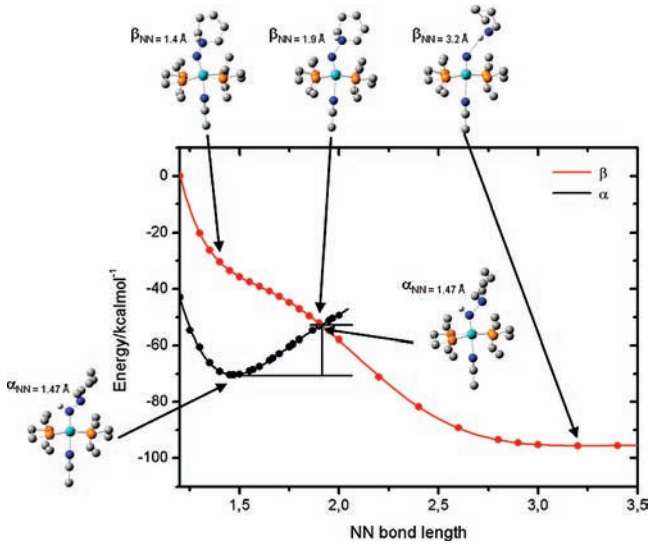

Figure 8. Energies of the α-protonated (black) and the *β*-protonated (red) model complex $\mathbf{B}_{dmpe}$ calculated from DFT as a function of the NN-bond length. The complexes are presented without alkyl-Hs.

(4) The N_β-protonated, solvent-coordinated intermediate **MeCN-BH**$^+$ spontaneously decays into the nitrido complex **MeCN-Mo≡N** and piperidine, cleaving the N−N bond. However no rPES was performed for this reaction.

(5) The doubly (at N_α and N_β) protonated, solvent coordinated intermediate **MeCN-BH$_2$**$^{2+}$ also spontaneously cleaves the N−N bond, generating the imido complex **MeCN-Mo≡NH** and piperidine. For this reaction a rPES was performed, again showing a barrierless profile between the doubly protonated dialkylhydrazido complex and the products (imido complex + piperidine).[29]

These results can be summarized in such a way that a N_β-protonated intermediate *always* cleaves the N−N bond, with and without a second proton at N_α and in the presence and the absence of a coordinated solvent molecule. In contrast, when the complex is *only* protonated at N_α, it appears to be inert toward N−N cleavage. To check whether this also holds for the solvent-coordinated, N_α protonated complex (which was not treated by DFT in the earlier study) this intermediate was geometry optimized in the present study. To assess the stability of this intermediate toward N−N cleavage a rPES along the N−N coordinate was performed. As a matter of fact, an energy minimum at ∼1.5 Å and a monotonic energy increase at larger N−N bond distances is found (Figure 8). In the same figure the rPES for N−N cleavage of the N_β-protonated, solvent coordinated intermediate is shown. As expected, the energy profile for N_β protonation exhibits a monotonic decrease, corresponding to a barrierless N−N cleavage process. For small N−N distances, however, the N_β surface is at higher energy than the N_α surface, indicating that under these circumstances *N_α-protonation is energetically favored with respect to N_β-protonation*.

It thus may be possible that, *even if primary protonation occurs at N_β*, the proton after solvent coordination and bending shifts to N_α. In this configuration N−N cleavage is hindered. Only after elongation of the N−N bond up to the crossing point of the two surfaces can the proton be transferred back from N_α to N_β, allowing N−N cleavage to proceed. The 1,2-proton backshift thus effectively constitutes an activation barrier to the N−N cleavage reaction. This theoretically derived picture will become important when discussing the origin of the temperature-dependent N−N cleavage characteristics in the regime of low acid concentrations (see below).

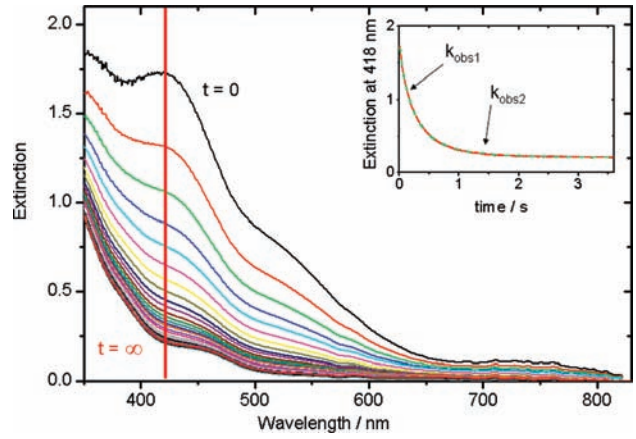

Figure 9. Time evolution of the UV/vis-spectra during the reaction of $\mathbf{B}^{Mo}$ ($c = 0.25$ mmolL^{-1}) with $HNEt_3BPh_4$ ($c = 20$ mmol L^{-1}) in acetonitrile at $T = 15$ °C. Six hundred spectra were recorded over a time period of $t = 3.6$ s. Each twelfth is shown. Inset: Time evolution of the extinction at 418 nm.

Table 7. Experimental Concentration-Dependent Rate Constants for the Two Observed Reaction Steps ($T = 15$ °C) in Comparison with the Rate Constants Found by Henderson et al.[27]

$[HNEt_3^+]$/(mmol/L)	$k_{obs(1)}$	$k_{obs(2)}$	$k_{Henderson}$[27]
1	3.2 ± 0.1	0.67 ± 0.05	15
5	4.0 ± 0.2	0.90 ± 0.07	∼40
10	4.6 ± 0.2	1.32 ± 0.07	∼50
20	6.1 ± 0.3	1.9 ± 0.1	58

B. Dependence of the N−N Cleavage Reaction on the Acid Concentration. Stopped-flow-measurements were performed; the reaction course was monitored with UV/vis spectroscopy to study the reaction of $\mathbf{B}^{Mo}$ with $HNEt_3BPh_4$ in acetonitrile. First the dependence of this reaction of the acid concentration was investigated at a constant temperature. Afterward measurements of the temperature dependence of the N−N cleavage reaction were performed. Figure 9 shows the evolution of the UV/vis spectra during the reaction of $\mathbf{B}^{Mo}$ with $HNEt_3BPh_4$ ($c = 20$ mmol L^{-1}) in acetonitrile at 15 °C. In the observed time period of 3.6 s 600 spectra were recorded, only a subset of these is shown in Figure 9.

The stopped-flow-measurements show the initial UV/vis spectrum of the complex and a fast decay of the optical band at 418 nm which almost completely disappears within 3 s. So we are able to monitor the reaction from the spectrum of the reactant until it is completed. The time evolution of the absorbance at 418 nm cannot be described by a mono-exponential behavior but can only be fitted to a bi-exponential behavior, indicating two consecutive reaction steps with observed rate constants $k_{obs(1)}$ and $k_{obs(2)}$. The first reaction is faster (about 3 times) than the second one. Interestingly, for all acid concentrations much smaller

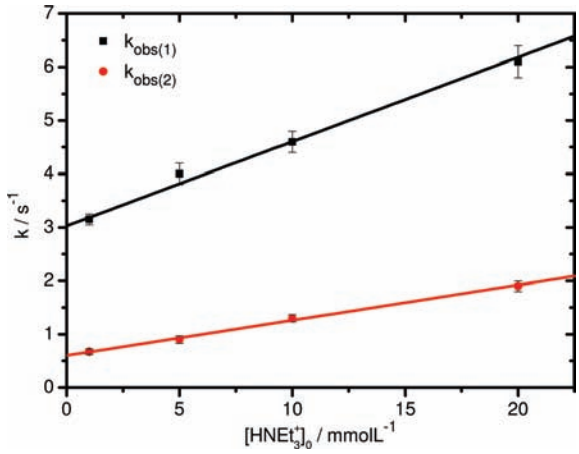

Figure 10. Rate constants for the first (k_1) and the second (k_2) reaction steps for the reaction of $\mathbf{B}^{Mo}$ with different acid concentrations. $T = 15$ °C.

rate constants are found (up to 1 order of magnitude) than determined for the single rate constant k_{obs} determined by Henderson et al. (Table 7).[27]

A plot of $k_{obs(1)}$ and $k_{obs(2)}$ against the acid concentration indicates linear dependences with slopes k_{1s} and k_{2s} and intercepts k_{1i} and k_{2i} shown in Figure 10:

$$k_{obs(1)} = k_{1i} + k_{1s} \cdot [HNEt_3^+]_0$$

$$k_{obs(2)} = k_{2i} + k_{2s} \cdot [HNEt_3^+]_0$$

From a linear regression fit the following values are determined at 15 °C:

$$k_{1i} = 3.03 \pm 0.07\ s^{-1}, \quad k_{1s} = 158 \pm 11\ M^{-1}\ s^{-1},$$

$$k_{2i} = 0.60 \pm 0.03\ s^{-1}, \quad k_{2s} = 65 \pm 3\ M^{-1}\ s^{-1}$$

The large intercept for both reaction steps is in agreement with a considerable part of the reaction being independent of the acid concentration because the reactive species is already in the protonated form. So we can derive an acid-independent rate constant k_i which is represented by the intercept and an acid-dependent rate constant k_s which is taken from the slope of the plots in Figure 10.

On the basis of the reactions shown in Scheme 2, these findings can be interpreted in the following way: again it is assumed that the first protonation step is very rapid; that is, is complete within the dead time of the stopped-flow apparatus.[40] Subsequently the solvent attacks; this would correspond to the rate constant $k_{obs(1)}$. The second rate constant, $k_{obs(2)}$, then corresponds to the actual N−N-cleavage step. These results would indicate that we are able to monitor *both* the coordination of the solvent *and* the cleavage of the N−N bond, in analogy to the W system and in contrast to the results obtained by Henderson et al. on $\mathbf{B}^{Mo}$, where only the last step was observed. In agreement with Henderson et al., on the other hand, the last process would have an acid-dependent and an acid-independent component, as represented by k_4 and k_5 in Scheme 1.

C. Derivation of Rate Equations. The above relations for $k_{obs(1)}$ and $k_{obs(2)}$ can straightforwardly be reproduced if we assume a clean two-step reaction proceeding as

$$\{B\}(\text{reactant}) \xrightarrow{k_{obs(1)}} \{C\}(\text{intermediates}) \xrightarrow{k_{obs(2)}} \{D\}(\text{products})$$

{B}, {C}, and {D} are cumulative designations for the five-coordinate hydrazido complex **B**, the solvent-coordinated intermediate **C** (= **MeCN-BH**$^+$) and the nitrido complex **D** (= **MeCN-Mo≡N**), as well as their respective protonated forms (**BH**$^+$, **BH$_2$**$^{2+}$, **CH**$^+$, **DH**$^+$). We assume that the protonations are rapid with respect to the other elementary reactions and do not alter the optical properties of **B**, **C**, and **D**; that is, **B**, **BH**$^+$, and **BH$_2$**$^{2+}$ are assumed to have the same absorption spectra.[41] The same holds for **C** and **CH**$^+$, as well as for **D** and **DH**: in all **C** intermediates, the hybridizations of N_α and N_β stay the same; for this reason the spectra probably are very similar, in agreement with the fact that only one "**C**" spectrum is observed at all acid concentrations (cf. Experimental Procedures). The spectra of the products "**D**" (nitrido and imido complex), finally, should also exhibit little difference (the n→π^* transition changes somewhat in energy, but its intensity is low.) $k_{obs(1)}$ thus would describe the cumulative conversion from {B} to {C} (i.e., solvent

Scheme 2

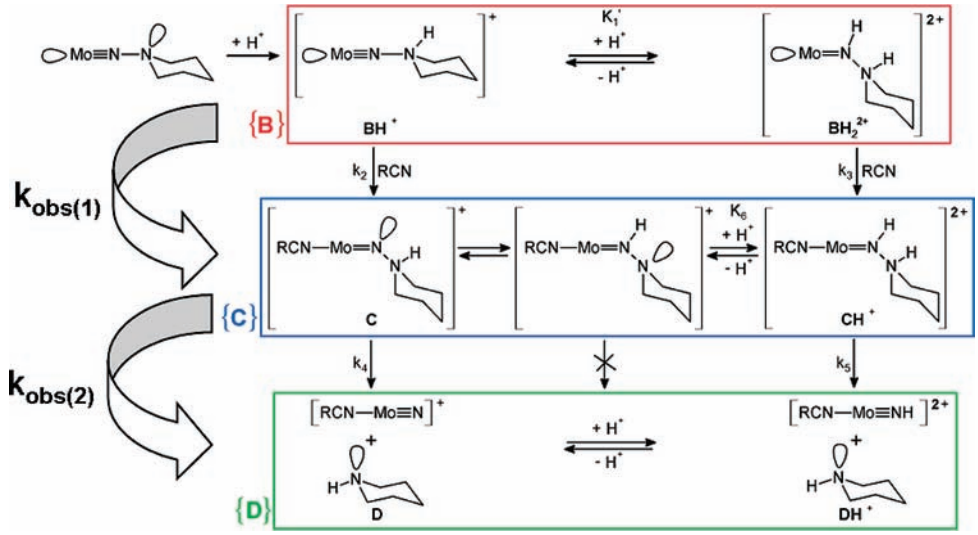

coordination) and $k_{obs(2)}$ the cumulative conversion of {C} to {D} (i.e., N−N cleavage).

For the conversion {B} → {C} we again refer to Scheme 2. Taking into account the two reaction channels leading from {B} via k_2 and k_3 to {C}, the time dependence of the total concentration of **C**, $[C]_{tot} = [C] + [CH^+]$, is given by

$$\frac{d[C]_{tot}}{dt} = k_2[RCN][BH^+] + k_3[RCN][BH_2^{2+}]$$

where RCN denotes the solvent (acetonitrile or propionitrile).

The equilibrium between the mono- and the diprotonated form of compound B is described by

$$K_1' = \frac{[BH_2^{2+}][NEt_3]}{[BH^+][HNEt_3^+]}$$

With $k_2[RCN] = k_2'$ and $k_3[RCN] = k_3'$ we have

$$\frac{d[C]_{tot}}{dt} = \left(k_2' + k_3'K_1'\frac{[HNEt_3^+]}{[NEt_3]}\right)[BH^+]$$

which is transformed with

$$[B]_{tot} = [BH^+] + [BH_2^{2+}] = [BH^+]\left(1 + K_1'\frac{[HNEt_3^+]}{[NEt_3]}\right)$$

into

$$\frac{d[C]_{tot}}{dt} = \left(k_2' + k_3'K_1'\frac{[HNEt_3^+]}{[NEt_3]}\right)\frac{[B]_{tot}}{1 + K_1'\frac{[HNEt_3^+]}{[NEt_3]}}$$

$$= \left(\frac{k_2'}{1 + K_1'\frac{[HNEt_3^+]}{[NEt_3]}} + \frac{k_3'K_1'\frac{[HNEt_3^+]}{[NEt_3]}}{1 + K_1'\frac{[HNEt_3^+]}{[NEt_3]}}\right)[B]_{tot} = -\frac{d[B]_{tot}}{dt}$$

We consider the case

$$K_1'\frac{[HNEt_3^+]}{[NEt_3]} = \frac{[BH_2^{2+}]}{[BH^+]} \ll 1$$

From the initial, complete protonation step and the fact that the secondary protonation equilibrium constant is small, we can further set

$$\frac{[HNEt_3^+]}{[NEt_3]} \cong \frac{[HNEt_3^+]_0 - [B]_0}{[B]_0} \cong \frac{[HNEt_3^+]_0}{[B]_0}$$

with $[HNEt_3^+]_0$ representing the initial acid concentration and $[B]_0$ the initial complex concentration (compound **B**). The decay of the reactant **B** in the first phase of the reaction thus is determined by

$$-\frac{d[B]_{tot}}{dt} \cong \left(k_2' + k_3'K_1'\frac{[HNEt_3^+]_0}{[B]_0}\right)[B]_{tot}$$

$$\equiv (k_{1i} + k_{1s}[HNEt_3^+]_0)[B]_{tot} = k_{obs(1)}[B]_{tot}$$

as found experimentally, with $k_{1i} = k_2[RCN]$ and $k_{1s} = k_3[RCN]\ K_1'/[B]_0$.

For the second reaction step {C} → {D} we also refer to Scheme 2. Note that k_4 and k_5 are now true first-order rate constants and do not involve the solvent any more. Correspondingly, the following relation holds:

$$\frac{d[D]_{tot}}{dt} = k_4[C] + k_5[CH^+]$$

or with the equilibrium between the solvent-coordinated, monoprotonated intermediate **C** and its doubly protonated form, $\mathbf{CH}^+$, given by

$$K_6 = \frac{[CH^+][NEt_3]}{[C][HNEt_3^+]}$$

and the relation $[C]_{tot} = [C] + [CH^+]$ (vide supra):

$$\frac{d[D]_{tot}}{dt} = \left(k_4 + k_5K_6\frac{[HNEt_3^+]}{[NEt_3]}\right)\frac{[C]_{tot}}{1 + K_6\frac{[HNEt_3^+]}{[NEt_3]}} = -\frac{d[C]_{tot}}{dt}$$

Analogous to the first reaction step we consider the case

$$K_6\frac{[HNEt_3^+]}{[NEt_3]} = \frac{[CH^+]}{[C]} \ll 1$$

With the same approximations as above,

$$\frac{[HNEt_3^+]}{[NEt_3]} \cong \frac{[HNEt_3^+]_0 - [B]_0}{[B]_0} \cong \frac{[HNEt_3^+]_0}{[B]_0}$$

the overall decay of the intermediate species C is determined by the rate equation

$$-\frac{d[C]_{tot}}{dt} = \left(k_4 + k_5K_6\frac{[HNEt_3^+]_0}{[B]_0}\right)[C]_{tot}$$

$$\equiv (k_{2i} + k_{2s}[HNEt_3^+]_0)[C]_{tot} = k_{obs(2)}[C]_{tot}$$

as observed experimentally, with $k_{2i} = k_4$ and $k_{2s} = k_5\ K_6/[B]_0$.

D. Temperature Dependence and Activation Parameters. For the determination of the temperature dependence of the N−N cleavage reaction we have to distinguish between reaction channels which depend on the acid concentration and those which are acid-independent. For the latter type of reactions the temperature dependence of the corresponding rate constants (i.e., k_{1i} and k_{2i}) should obey the Eyring equation

(40) Importantly, the "initial" spectrum at $t \rightarrow 0$ (intermediate $\mathbf{BH}^+$) corresponds to that of intermediate **B**. The fact that we observe a first-order decay of this initially prepared species in the first phase of the reaction suggests that this species must already be protonated (as compound **B** is stable in the absence of acid). Moreover, the fact that we observe N−N cleavage that does not show acid dependence (from the intercept of $k = f([HNEt_3^+]_0)$) is in favor of the initial rapid protonation, since without protonation the reaction would not occur.

(41) The absorption spectrum of the initially prepared species, $\mathbf{BH}^+$, is identical to that of compound **B** as the hybridization of N_α and N_β, as well as the electronic structure of the central Mo(II) center, do not change upon protonation of N_β. This is different in case of the doubly protonated, bent intermediate $\mathbf{BH_2}^{2+}$ which therefore also should have a different spectrum to that of **B** and $\mathbf{BH}^+$. However, our kinetics suggest that K'_1 has a very small value; that is, the amount of $\mathbf{BH_2}^{2+}$ that can be present in the initial solution most probably is negligible even at the highest acid concentrations that were applied.

$$\ln\left(\frac{k}{T}\right) = \ln\left(\frac{k_B}{h}\right) + \frac{\Delta S^{\ddagger}}{R} - \frac{\Delta H^{\ddagger}}{RT}$$

and a plot of ln (k/T) versus $1/T$ should give $23.76 + \Delta S^{\ddagger}/8.31$ as intercept and $\Delta H^{\ddagger}/8.31$ as slope.

The N−N cleavage of the doubly protonated intermediate $\mathbf{CH}^+$ (cf. Scheme 2) involves a pre-equilibrium which corresponds to K_6, so k_{2s} is composed of the equilibrium constant and the rate constant of the N−N splitting.; that is, $k_{2s} = k_5K_6/[B]_0$ (vide supra) or

$$\ln(k_{2s}) = \ln(k_5/[B]_0) + \ln(K_6) = \ln(k_5/[B]_0) + \frac{\Delta S_6^0}{R} - \frac{\Delta H_6^0}{RT}$$

DFT calculations suggest that N−N cleavage via k_5 does not involve a major thermal barrier, that is, it should be rather temperature-independent (cf. Section A).[42] The temperature dependence of k_{2s} thus should predominantly be determined by the temperature dependence of K_6, and a plot of $\ln(k_{2s})$ versus $1/T$ should give $\ln(k_5/[B]_0) + \Delta S_6^0/R$ as intercept and $-\Delta H_6^0/R$ as slope. The acid-dependent part of the first reaction step ($\mathbf{BH_2}^{2+} \rightarrow \mathbf{CH}^+$, cf. Scheme 2) also formally involves a protonation pre-equilibrium (K_1'). However, in this case the subsequent reaction step (solvent attack) cannot a priori be assumed to proceed without a thermal barrier. We therefore can only evaluate the activation barrier for the *combined* reaction (protonation and solvent attack) from an Eyring plot of k_{1s}, in analogy to k_{1i} and k_{2i}.

To determine these parameters, temperature-dependent stopped-flow measurements were performed. Plots of $\ln(k_{1i}/T)$, $\ln(k_{1s}/T)$, $\ln(k_{2i}/T)$, and $\ln(k_{2s})$ versus $1/T$, where k_s has been obtained from the slope of the concentration dependent plots at different temperatures and k_i from the intercepts, are given in Figure 11. From a regression analysis of $\ln(k_{1i}/T)$ versus $1/T$ the following activation parameters associated with k_2 wer e obtained: $\Delta S_2^{\ddagger} = -128 \pm 17$ J mol^{-1} K^{-1} and $\Delta H_2^{\ddagger} = 31 \pm 4$ kJ mol^{-1}. For ln (k_{1s}/T) versus $1/T$ the same analysis gave the activation parameters associated with k_3 (and K_1'): $\Delta S_3^{\ddagger} = -122 \pm 45$ J mol^{-1} K^{-1} and $\Delta H_3^{\ddagger} = 23 \pm 12$ kJ mol^{-1}. The activation parameters associated with k_4, obtained from a fit of $\ln(k_{2i}/T)$ versus $1/T$, were determined to $\Delta S_4^{\ddagger} = -102 \pm 4$ J mol^{-1} K^{-1} and $\Delta H_4^{\ddagger} = 42 \pm 1$ kJ mol^{-1}. We thus obtained for all mentioned processes activation enthalpies in the range of 20 to 40 kJ mol^{-1} and activation entropies in the range of −100 to −130 J mol^{-1} K^{-1}. For the acid-dependent part of the N−N cleavage described by k_{2s} (k_5-pathway), on the other hand, we find from a plot of $\ln(k_{2s})$ versus $1/T$: $\Delta H_6^0 = 36 \pm 4$ kJ mol^{-1} and $\ln(k_5/[B]_0) + \Delta S_6^0/R = 20 \pm 2$. The entropy of the equilibrium K_6 cannot be determined independently, but the corresponding reaction enthalpy is positive, suggesting an endergonic protonation equilibrium.

E. Interpretation of Results and Formulation of a Revised Mechanistic Scheme. To account for these results, the modified reaction scheme given in Scheme 2 is used. In general, cleavage of the N−N bond requires only one proton, whereby we assume that for steric reasons this proton is initially coordinated to N_β (vide infra). If no further proton is added (limiting case of small $[HNEt_3^+]_0$), the subsequent reaction pathway is determined by k_2 and k_4. Solvent coordination in the low acid concentration range (k_2) is temperature-dependent because the N_β-protonated intermediate initially exhibits a linear Mo−N−N-unit with a lone-pair at the metal center. Coordination of a Lewis base at this position therefore is not possible and can only occur if the protonated intermediate bends at N_α, which constitutes an activation barrier (the DFT calculation gives a barrier of 17 kcal/mol (71 kJ/mol) for this process, vide supra). The temperature-dependent behavior of k_2 thus can be understood on the basis of a primary protonation at N_β. If, in contrast, primary protonation of compound **B** occurred at N_α, the protonated intermediate would spontaneously bend at N_α and solvent coordination would involve a much smaller activation barrier. More importantly, in this case also the $[HNEt_3^+]_0$ dependence of $k_{obs(1)}$ would be difficult to understand, as a second protonation at N_β would *not* change the geometry of the five-coordinate, bent complex and thus would *not* act to lower a possibly existing barrier for solvent coordination.

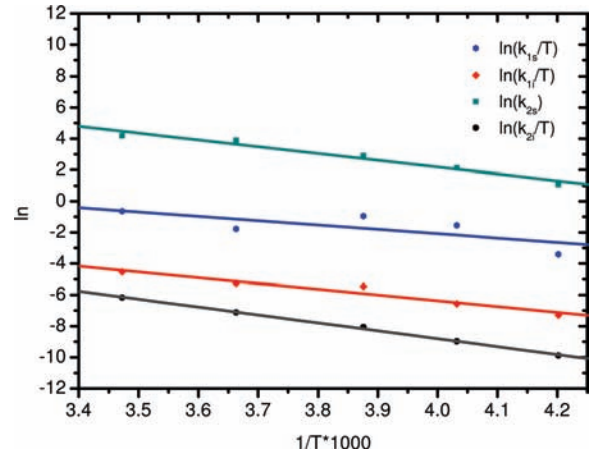

Figure 11. Plot of $\ln(k_{1s}/T)$, $\ln(k_{1i}/T)$, $\ln(k_{2s})$, and $\ln(k_{2i}/T)$ against $1/T \times 1000$ with the linear regression lines.

As described earlier, the temperature-dependent behavior of the N−N cleavage process in the low acid concentration range (rate constant k_4) can be explained by the existence of an N_α-protonated intermediate (all N_β-protonated intermediates cleave the N−N bond spontaneously). After the first protonation of intermediate B at N_β, subsequent bending and solvent attack, the proton thus shifts rapidly from N_β to N_α, precluding N−N cleavage. Splitting of the N−N bond can only occur if the proton shifts back to N_β, which is associated with an activation energy. Alternatively, another proton can be added at N_β (requiring higher acid concentrations), which also leads to N−N cleavage. The latter pathway accounts for the increase of $k_{obs(2)}$ via k_{2s} (k_5). A second proton (this time at N_α) may already be added at the level of the solvent-free intermediate $\mathbf{BH}^+$; this accounts for the increase of $k_{obs(1)}$ via k_{1s} (k_3): if a second proton is added to the solvent-free intermediate at N_α, it spontaneously bends, thus facilitating

(42) Notably, this is a gas-phase result, and more elaborate treatments including intermolecular interactions and solvent effects may provide evidence for some barriers for N−N cleavage. These, however, should be small and, in particular, in view of the large exothermicity of the N−N cleavage, should not alter the validity of the above statement.

solvent coordination. The temperature-dependent characters of k_{1s} and k_{2s} reflect the corresponding endergonic protonation equilibria K_1 and K_6, respectively.

The most interesting part of the revised reactive scheme is the double 1,2-proton shift from N_β to N_α and back in the limit of low acid concentrations. The energy profile for the proton backshift is shown in Figure 8. The potential energy curves cross at an N−N bond length of 1.9 Å, where the proton can shift isoenergetically from $\alpha \rightarrow \beta$. Starting from the geometry optimized, N_α protonated geometry the estimated barrier for this process is 17.5 kcal mol^{-1} (73 kJ mol^{-1}). This is significantly higher than determined experimentally as activation barrier for N−N cleavage in the low [$HNEt_3^+$] regime (42 kJ mol^{-1}, see above). A possible explanation for this discrepancy might be the fact that proton transfer from N_α to N_β is catalyzed by a second proton, significantly lowering the activation energy for this process. The theoretically derived value of 73 kJ mol^{-1}, in contrast, represents a lower limit for the activation energy of the *uncatalyzed* proton shift from N_α to N_β.

V. Discussion

A. Comparison between B^{Mo} and B^{W}. In the preceding sections experimental and theoretical investigations on the reaction of the Mo-dialkylhydrazido complex $\mathbf{B}^{Mo}$ with acid have been presented. Both the Mo complex and its W counterpart $\mathbf{B}^{W}$ show biphasic N−N cleavage kinetics, which in the framework of Henderson's original mechanistic scheme can be explained with a rapid protonation within the dead time of the stopped-flow apparatus, subsequent coordination of the solvent, and a slow cleavage of the N−N bond. For the Mo complex $\mathbf{B}^{Mo}$, however, our rate constants are significantly smaller than the single rate previously reported.[27] In any case, the W complex $\mathbf{B}^{W}$ reacts orders of magnitude faster than its Mo counterpart. Moreover, no dependence of the rates on the acid concentration was found for the tungsten complex; that is, in this case the protonation equilibria are already saturated at a small excess of acid. This indicates a higher basicity of the W complex which is also borne out by structural parameters such as a larger N−N bond length, a smaller metal-N bond length, and a larger pyramidalization of the terminal N-atom, similar to $N-NR_2$ complexes of early transition metals.[43] The main vibrational-spectroscopic consequences of these structural differences are small shifts of the metal-N vibrations of $\mathbf{A}^{Mo}$ and $\mathbf{B}^{Mo}$ toward smaller frequencies as compared to those of their tungsten counterparts, indicating slightly weaker metal-N bond strengths. In the region of the N−N vibrations, however, no systematic frequency shifts are detectable. This is probably due to the large degree of mixing between the N−N stretch and the modes of the piperidine ring, blurring differences in N−N bonding between the Mo and W systems.

The main goal of this paper was an understanding of the strong temperature dependence of the N−N cleavage rate of $\mathbf{B}^{Mo}$ and $\mathbf{B}^{W}$. For the latter complex the reaction rate was found to be very fast at room temperature and only at −70 °C became amenable to stopped-flow kinetics. To determine activation parameters for N−N cleavage we therefore had to go to the "slower" complex $\mathbf{B}^{Mo}$ which in this study was investigated by stopped-flow kinetics in the temperature range between −35 and +15 °C. The two phases of the reaction could be divided into an acid-independent and an acid-dependent component each. The strong temperature dependence of the overall reaction was traced back to the activation enthalpies and negative activation entropies for three involved reaction channels. For the fourth reaction channel an endergonic pre-equilibrium was found. The activation barriers for the first reaction phase corresponding to $k_{obs(1)}$ are attributed to solvent coordination at low and higher acid concentrations. The activation barriers for the second phase corresponding to $k_{obs(2)}$ are associated with details of the N−N cleavage process. The temperature-dependent behavior at *high* acid concentrations derives from an endothermic pre-equilibrium. The activation barrier for N−N cleavage at *low* acid concentrations is attributed to an N_α-protonated intermediate that is inert to N−N cleavage. This species is in turn generated by a rapid 1,2-proton shift from an N_β protonated intermediate with a coordinated solvent molecule. For N−N cleavage of the singly, α-protonated intermediate the proton has to shift back from N_α to N_β, which constitutes the activation barrier observed for this step. In the presence of higher acid concentrations the N_α protonated intermediate adds a second proton at N_β, leading to a doubly protonated intermediate which spontaneously cleaves the N−N bond. In the case of $\mathbf{B}^{Mo}$ this equilibrium is endergonic, accounting for the temperature-dependent N−N cleavage observed for the former complex in the regime of higher acid concentrations.[44]

Besides the consecutive pathway (B → C → D) employed to account for the biphasic kinetics, three alternative scenarios are conceivable all of which are based on two competitive reaction channels:

(i) simultaneous generation and decay of a single and a double protonated intermediate;

(ii) simultaneous generation and decay of a N_α and a N_β protonated intermediate;

(iii) simultaneous generation and decay of a solvent-coordinated and solvent-free intermediate.

Scenario (i): if this scenario was correct, the kinetics would become monophasic at very small and very large acid concentrations, corresponding to exclusive decay via a monoprotonated and a diprotonated intermediate, respectively. This, however, is not observed; that is, the decay is biphasic at all acid concentrations.

Scenario (ii): as we know from DFT that N−N cleavage following N_α protonation has a large barrier, whereas N−N cleavage after N_β protonation has no barrier, drastically

(43) Selby, J. D.; Manley, C. D.; Feliz, M.; Schwarz, A. D.; Clot, E.; Mountford, P. *Chem. Commun.* **2007**, 4937–4939.

(44) The activated characteristics of the acid-dependent pathways could also be associated with rate-limiting protonation reactions. This would be evident from deuterium effects. We have looked for this, employing the deuterated acid $DNEt_3^+$, but found that the rate constants were not affected.

Scheme 3

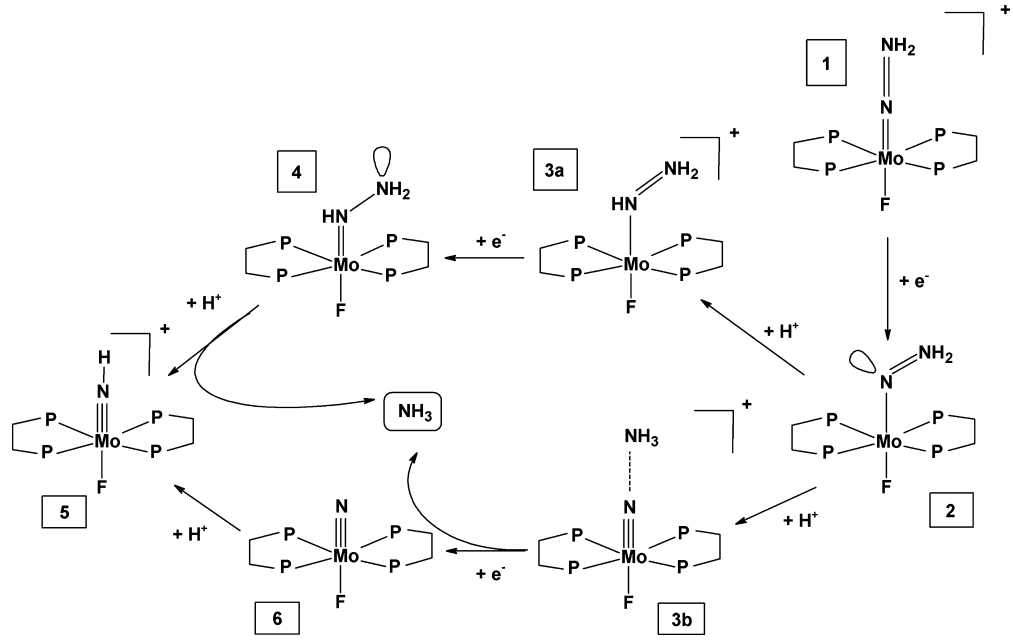

different activation parameters for both competing N−N cleavage channels should be observed. This, however, is not the case.

Scenario (iii): as we know from DFT that the N_β-protonated, solvent-free intermediate also cleaves the N−N bond without barrier, this is indeed a viable scenario. However, it is already known from Henderson's investigation that the rate of the N−N cleavage process markedly depends on the nitrile. In case of the tungsten dialkylhydrazido complex $\mathbf{B}^{W}$ we noticed that in benzonitrile solution N−N cleavage is hindered and a long-lived intermediate (probably a W−NNR_2 benzonitrile complex) is observed. We therefore assume that in nitrile solvents the direct N−N cleavage path is overruled by solvent coordination, and N−N cleavage only takes place in the solvent-coordinated complex. This scenario also makes sense in view of the fact that the second reaction phase (which must involve N−N cleavage) is much slower than the first phase. If both reaction phases were associated with N−N cleavage processes we would assume that, at least at high acid concentrations, their rates become similar. This, however, is not observed.

The mechanism shown in Scheme 2, in contrast, provides a coherent and complete picture of the acid and temperature dependence of the N−N cleavage of both $\mathbf{B}^{Mo}$ and $\mathbf{B}^{W}$ and resolves the mechanistic problems encountered in the previous study. From the initial DFT calculations all N−N cleavage processes appeared to be barrierless; therefore the strong temperature dependence was difficult to understand. Now we have determined and theoretically interpreted the barriers in the overall reaction scheme leading to the observed temperature dependence and thus have obtained additional insight into the mechanistic details of the seemingly simple N−N cleavage reaction of compound **B**.

B. Relevance to the Chatt Cycle. Although compounds $\mathbf{B}^{Mo}$ and $\mathbf{B}^{W}$ have been prepared from their metal(IV) precursors by synthetic means which are not related to the Chatt cycle, the N−N cleavage upon reaction with acids is of direct relevance to this reactive scheme, as is shown now. In the *classic* Chatt cycle, a Mo or W bis(dinitrogen) complex is protonated with mineral acid, exchanging one dinitrogen ligand by an anionic base; for example, fluoride. A key intermediate in the first phase of the Chatt cycle is the Mo(IV) hydrazido(2-) complex (Scheme 3, **1**).[45] According to our DFT analysis of the classic Chatt cycle,[46] this intermediate is first reduced to the bent Mo(III) HN=NH_2 complex **2**, which can be protonated at N_α or N_β. In the former case a bent Mo(III) $HNNH_2$ complex (**3a**) is generated which in a final electron transfer step is converted to the bent Mo(II) $HNNH_2$ complex **4**. Upon final protonation at N_β this complex cleaves the N−N bond and generates NH_3, in analogy to the doubly protonated compounds $\mathbf{B}^{Mo}$ and $\mathbf{B}^{W}$. If the bent Mo(III) N=NH_2 complex **2** is protonated at N_β, it linearizes again, forming the Mo(III) NNH_3 complex **3b** with an extremely elongated N−N bond. Upon final reduction of this complex to the Mo(II) species the N−N bond is cleaved, generating NH_3 as well. The existence of the linear Mo(III) hydrazidium complex, however, is due to the stabilizing influence of the *trans*-fluoro ligand; this species is not observed if the anionic *trans* ligand is replaced by neutral donor such as N or P.

This is the case for the *modified* Chatt cycle which applies to complexes having a phosphine moiety in the *trans*-position to N_2; for example, [Mo(N_2)(dpepp)(dppm)] (dpepp = bis(diphenylphosphinoethyl)phenylphosphine; dppm = 1,2-bis(diphenylphosphino)methane). This complex was first

(45) DFT and spectroscopy rather suggest a Mo(II) isodiazene formulation for this complex, cf. refs 16 and 17. In the literature, however, these complexes are denoted as Mo(IV) hydrazido(2-) complexes, and we will adhere to this convention here. Also in the following discussion, alternative valence descriptions of the Mo-NNH_x intermediates are possible; cf. refs 46 and 52.

(46) Stephan, G. C.; Sivasankar, C.; Studt, F.; Tuczek, F. *Chem. Eur. J.* **2008**, *14*, 644–652.

Table 8. Energies of the Intermediates of Protonation and Reduction Based on DFT Calculations[a]

	Chatt cycle (cf. Scheme 3) intermediate #	relative energy (kcal/mol)	modified Chatt cycle (cf. Scheme 4) intermediate #	relative energy (kcal/mol)
$[Mo{=}N{=}NH_2]^{+/2+}$	**1**	0.0	**1′**	0.0
$[Mo{=}N{=}NH_2]^{0/+}$	**2**	−16.4	**2′**	−26.7
$[Mo(HN{=}NH_2)]^{+/2+}$	**3a**	−23.6	**3a′**	−29.5
$[Mo(N{-}NH_3)]^{+/2+}$	**3b**	−13.9	**3b′**	−14.8
$[Mo(HN{-}NH_2)]^{0/+}$	**4**	−88.1	**4′**	−102.6
$[Mo{\equiv}NH]^{+/2+}$	**5**	−172.9	**5′**	−166.4
$[Mo{\equiv}N]^{0/+}$	**6**	−154.1	**6′**	−160.6

[a] acid = protonated ether, reductant = Cp^*_2Cr; cf. Schemes 3 and 4; for details see refs 47 and 53.

Scheme 4

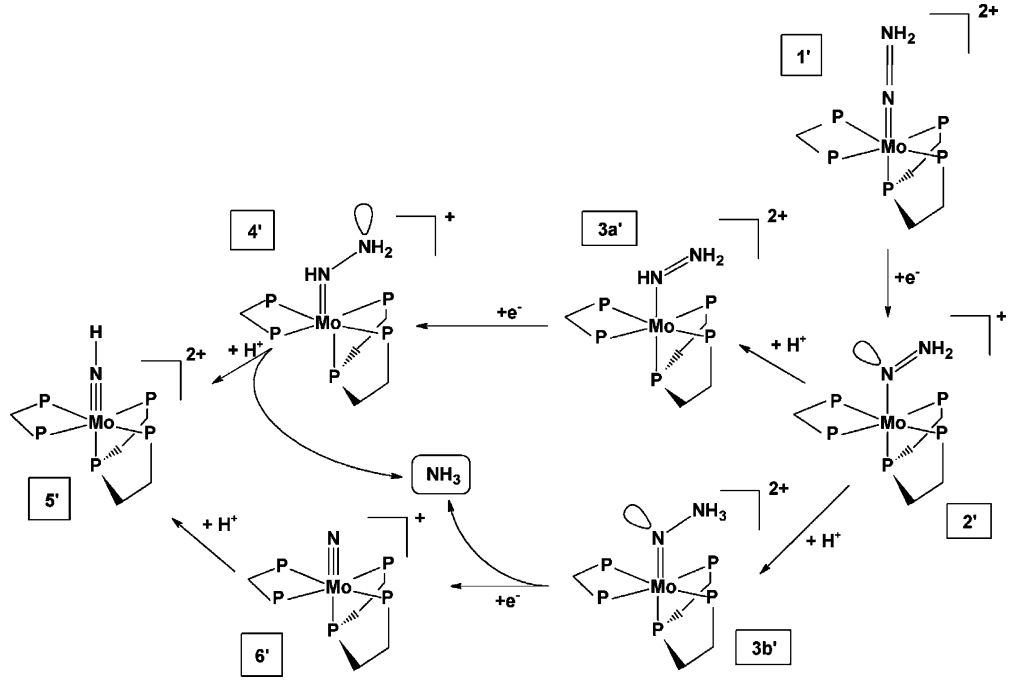

prepared and characterized by George et al.,[47−49] who also showed that protonation of the N_2 ligand is possible with retention of the *trans*-phosphine group. We have extensively investigated this and related complexes with DFT and spectroscopy[50,51] and have performed DFT calculations to evaluate the energetics of a possible catalytic cycle on the basis of this system.[52] The energetics of the classic and modified Schrock cycles based on decamethylchromocene as a reductant and lutidinium as acid are compared in Table 8. Also for the modified Chatt cycle, we consider the hydrazido(2-) derivative of $[Mo(N_2)(dpepp)(dppm)]$ as the starting point of the N−N cleavage process (Scheme 4, **1′**). According to the DFT analysis of the reactive pathway this complex is first reduced, generating the bent Mo(III) hydrazido(2-) intermediate **2′** which can be protonated at N_α or N_β. In the former case protonation leads to a bent Mo(III) $HN{=}NH_2$ complex (**3a′**). Further reduction generates the bent Mo(II) analogue (**4′**) which upon final protonation to a Mo(II) $HN{-}NH_3$ intermediate cleaves the N−N bond. Alternatively, if the bent Mo(III) hydrazido(2-) complex is β-protonated, it generates a bent Mo(III) NNH_3 complex (**3b′**). Upon one-electron reduction of this complex to the bent Mo(II) NNH_3 intermediate the N−N cleavage occurs as well. The β-protonated Mo(II) NNH_3 complex thus cleaves the N−N bond spontaneously whereas the α-protonated Mo(II) $HN{-}NH_2$ isomer needs a further proton to split the N−N bond. This exactly corresponds to the reactivities evidenced for the alkylated complexes $\mathbf{B}^{Mo}$ and $\mathbf{B}^{W}$ (note that the corresponding hydrazidium intermediates also have a neutral - nitrile - ligand in *trans*-position). The minimum requirement for N−N cleavage in the Chatt cycle therefore is a bent Mo(II) NNH_3 moiety; with a lower degree of protonation and/or a higher oxidation state of the metal center, the N−N bond is inert to cleavage.

C. Relevance to Nitrogenase. The mechanistic information obtained in this paper is also of relevance to the mechanistic pathway of dinitrogen reduction in nitrogenase. A basic question in this regard has been whether dinitrogen binds at the molybdenum center or at the iron centers of the central Fe_6 prism.[53] Moreover, there has been a continuing

(47) George, T. A.; Kovar, R. A. *Inorg. Chem.* **1981**, *20*, 285–287.
(48) George, T. A.; Ma, L.; Shailh, S. N.; Tisdale, R. C.; Zubieta, J. *Inorg. Chem.* **1990**, *29*, 4789–4796.
(49) George, T. A.; Tisdale, R. C. *Inorg. Chem.* **1988**, *27*, 2909–2912.
(50) Studt, F.; Tuczek, F. *Angew. Chem., Int. Ed.* **2005**, *44*, 5639–5642.
(51) Klatt, K.; Stephan, G.; Peters, G.; Tuczek, F. *Inorg. Chem.* **2008**, *47*, 6541–6550.
(52) Dreher, A.; Stephan, G.; Tuczek, F. In Metal Ion Controlled Reactivity; C. Hubbard, R. v. Eldik; Eds.; *Adv. Inorg. Chem.* 2009, Vol. 61, in press.
(53) Henderson, R. A. *Chem. Rev.* **2005**, *105*, 2365–2438.

debate as to whether the biological mechanism is analogous to the Chatt and Schrock cycles or follows a different path. In the latter case the reduction mechanism would in particular involve intermediates like diazene (HN=NH) or hydrazine (H_2N-NH_2) which do not appear in the Chatt cycle. To distinguish these two scenarios, the terms "D-mechanism" and "A-mechanism" have been introduced. These describe the fact that in the former case (D-mechanism) only the distal N-atom (N_β) of end-on terminally coordinated dinitrogen is protonated before N−N cleavage (as in the Chatt and Schrock cycles) whereas in the latter case (A-mechanism) the distal (N_β) *and* proximal N (N_α) are protonated in an alternating fashion.[54]

To obtain information on this issue methyldiazene, $HN=N-CH_3$, and its isotopomers labeled with ^{15}N at the terminal or internal nitrogens or with ^{13}C or ^{2}H were used as substrates for the nitrogenase $\alpha-196^{Gln}$-substituted MoFe protein (this mutagenesis specifically compromises proton delivery to the substrate).[54] EPR, as well as ^{1}H, ^{15}N and ^{13}C ENDOR, spectroscopic studies showed that a methyldiazene derived species in fact binds to the cofactor and coordinates through a [-NH_x] fragment. This was taken as evidence for the lack of a d-mechanism, where such a fragment supposedly cannot occur before N−N cleavage. The present investigation of the N−N cleavage of an $N=NR_2$ ligand, however, suggests that an α-protonated $HN-NR_2$ ligand may well play a role in the Chatt cycle. As described in the previous sections, it is generated from the initially formed β-protonated $N-NR_2H$ intermediate by a rapid 1,2-proton shift as a thermodynamically favorable species which, however, is inert to N−N cleavage. Thus it may be anticipated that in a rapid freeze-quench experiment under limited proton supply *this* (and not the β-protonated) intermediate is trapped. The low-temperature detection of an α-protonated intermediate prior to N−N cleavage thus may also be compatible with a Chatt-like ("d-" type) scenario and therefore cannot be taken as evidence for the presence of an "a-" type mechanism in the enzyme.

D. Conclusions. In summary, detailed mechanistic insight into a central step of nitrogen fixation, the cleavage of the N−N bond, has been obtained using a combination of kinetic, structural, and spectroscopic, as well as theoretical (DFT), investigations applied to Mo and W dialkylhydrazido(2-) complexes. The N−N cleavage of the six-coordinate, bent metal(II) dialkylhydrazidium species resulting from reaction of these complexes with acids in nitrile solvents represents a key step of the Chatt cycle which, although highly exothermic,[55] is associated with appreciable thermal activation barriers. For the Mo dialkylhydrazido complex $[MoL(NNC_5H_{10})(dppe)_2]$ (L = solvent) these barriers have been identified, and the corresponding activation parameters have been quantitatively determined, as well as theoretically interpreted on a molecular level.

Acknowledgment. F.T. thanks the Deutsche Forschungsgemeinschaft (DFG Tu58/14-2) for support of this research. A.D. thanks U. Cornelissen and Dr. G. Peters for help with the spectroscopic measurements. R.vE. and I.I.B. acknowledge financial support from DFG SFB 583 "Redox-active Metal Complexes".

Supporting Information Available: ^{1}H- and 45 °COSY NMR spectra of $\mathbf{A}^{Mo}$, time-dependent spectra of $\mathbf{B}^{Mo}$ after protonation. This material is available free of charge via the Internet at http://pubs.acs.org.

IC801952V

(54) Barney, B. M.; Lukoyanov, D.; Yang, T. C.; Dean, D. R.; Hoffman, B. M.; Seefeldt, L. C. *Proc. Natl. Acad. Sci. U.S.A.* **2006**, *103*, 17113–17118.

(55) In fact, this is the most exothermic step of the Chatt cycle (cf. refs 46 and 52) and the Schrock cycle (cf. ref 50).